

Danish Meteorological Institute

———— Scientific Report ——

98-2

The GPSOS project

**Algorithm Functional Design and Analysis
of Ionosphere, Stratosphere and Tropo-
sphere Observations**

By

**Per Høeg
Georg Bergeton Larsen
Hans-Henrik Benzon
Stig Syndergaard
Mette Dahl Mortensen**



Solar-Terrestrial Physics Division, Danish Meteorological Institute,
Lyngbyvej 100, DK-2100 Copenhagen Ø, Denmark

Table of Content

TABLE OF CONTENT.....	1
1. INTRODUCTION	3
2. NOMENCLATURE.....	4
3. REVIEW OF PHYSICS GOVERNING MEASUREMENTS	6
3.1 PHYSICAL FUNDAMENTALS	6
3.2 ATMOSPHERIC CONDITIONS.....	7
3.3 ELECTROMAGNETIC WAVE PROPAGATION IN THE ATMOSPHERE.....	8
4. MEASUREMENT METHODS AND TRADE-OFF	9
4.1 IONOSPHERIC MEASUREMENTS	9
4.1.1 SCINTILLATIONS	10
4.1.2 TOTAL ELECTRON CONTENT.....	12
4.1.3 IONOSPHERIC REFRACTIVITY	15
4.1.4 ELECTRON DENSITY	16
4.2 NEUTRAL ATMOSPHERIC MEASUREMENTS.....	18
4.2.1 NEUTRAL ATMOSPHERIC REFRACTIVITY	20
4.2.2 TEMPERATURE PROFILES.....	21
4.2.3 MOISTURE PROFILES.....	21
4.2.4 PRESSURE PROFILES.....	21
5. ALGORITHM DESCRIPTION	23
5.1 ON BOARD ALGORITHMS	23
5.1.1 AMPLITUDE SCINTILLATIONS.....	23
5.1.2 PHASE SCINTILLATIONS.....	23
5.1.3 SPECTRAL SCINTILLATION PROCESSING	25
5.2 POST PROCESSING ALGORITHMS	26
5.2.1 TOTAL ELECTRON CONTENT.....	26
5.2.2 IONOSPHERIC REFRACTIVITY RETRIEVAL.....	27

5.2.3	NEUTRAL ATMOSPHERIC REFRACTIVITY RETRIEVAL.....	28
5.2.4	ELECTRON DENSITY RETRIEVAL.....	30
5.2.5	TEMPERATURE, PRESSURE AND MOISTURE PROFILE RETRIEVAL	30
5.2.6	PRECIPITABLE WATER RETRIEVAL.....	31
6.	SYSTEM ERROR ANALYSIS.....	33
6.1	DEFINITION OF ATMOSPHERIC CONDITIONS	33
6.1.1	IONOSPHERE SCENARIOS.....	33
6.1.2	STRATOSPHERE/TROPOSPHERE SCENARIOS.....	34
6.2	ALGORITHM ERROR ASSESSMENT	35
6.2.1	SLANT TOTAL ELECTRON CONTENT (SLANT TEC)	35
6.2.2	ERROR BUDGET BASED ON DERIVED EQUATIONS AND SIMULATIONS	39
6.2.3	PRIMARY AND SECONDARY EDRS	41
6.2.4	RESULTS OF PRELIMINARY SIMULATIONS.....	43
6.2.5	PRELIMINARY SIMULATIONS OF ELECTRON DENSITY PROFILES.....	45
6.3	INSTRUMENT SENSITIVITY ANALYSIS.....	46
7.	REFERENCES.....	47
8.	FIGURE CAPTIONS	48
9.	FIGURES.....	51
APPENDIX A.....		77
APPENDIX B		79

1. Introduction

This scientific report defines the scope and requirements for the GPSOS (GPS/GLONASS Occultation Sensor) instrument, which is to be flown on all future US satellites launched in the NPOESS program.

NPOESS (National Polar-orbiting Operational Environment satellite system) reflects the united effort by NASA, NOAA (National Oceanic and Atmospheric Administration), DOE (Department of Energy) and DOD (Department of Defence) to monitor the whole atmosphere, from the troposphere and up to the ionosphere, from the future Earth observational satellite platforms. From year 2000 the NPOESS satellites will replace the DMSP and NOAA satellites in the series ending with DMPS S20 and NOAA N. In Europe the US NPOESS program will be complemented by the ESA/EUMETSAT missions consisting of the EPS/METOP satellites.

The report covers the science issues for the GPSOS system and necessary algorithms to be applied by the GPS limbsounding instrument, in order to observe the ionosphere electron density variations and structure together with the troposphere/stratosphere physical state.

In chapter 3 a short introduction to the physics of radio waves passing through the ionosphere and atmosphere is presented. Chapter 4 describes the algorithms needed to extract the information we wish to observe. The same algorithms are presented in more detail in chapter 5. Then in chapter 6 a preliminary analysis of the errors introduced in both algorithms and instrument is presented.

All figures are placed in the end of the document along with two appendices. Appendix A contains figures from another study by JPL (R. Kursinsky et. al 1997). Appendix B is a summary of the Primary and Secondary Environmental Data Records (EDR's) which are to be measured by the GPSOS sensor.

2. Nomenclature

L	carrier phase
\hat{L}	measured carrier phase
P	code phase
\hat{P}	measured code phase
$\Delta\Phi$	excess phase delay
N_e	electron density
B	phase ambiguity bias
B_0	earth's magnetic field strength
B_{\bullet}	horizontal component of the earth's magnetic field
ε	random error on carrier phase
ε_{gr}	random error on code phase
f	carrier frequency
w_i	weight factor
C	constant factor
K	constant factor
m	electron mass
e	electron charge
ϵ_0	permittivity of free space
θ	angle between ray -and magnetic field directions
cov	covarians function
corr	correlation function
σ_B	standard deviation on B
β_B	accuracy on B
β_R	ray path splitting bias term
β_{B_0}	second order ionosphere bias term
SNR	signal to noise ratio
	mean value over some finite time interval
$\Delta\beta$	clock errors
P	received signal power
S	signal phase
μ_{\bullet}	index of refraction
N	refractivity
t	time
τ	time lag
S_{pp}	spectral estimator
\bar{R}_L	position vector of the low earth orbit (LEO) satellite
\bar{R}_G	position vector of the GPS satellite
$\dot{\bar{R}}_L$	velocity vector of the low earth orbit (LEO) satellite

$\dot{\vec{R}}_G$	velocity vector of the GPS satellite
R_{LG}	the straight line distance between the LEO and the GPS satellite
a	impact parameter
z	height above earth's surface
R_{curve}	curvature radius at tangent point.
α	bending angle
φ	is the angle between incoming ray and the velocity of the LEO satellite
χ	is the angle between outgoing ray and the velocity of the GPS satellite
η	is the angle between position and velocity of the GPS satellite
ζ	is the angle between position and velocity of the LEO satellite
Θ	is the angle between the two position vectors

3. Review of Physics Governing Measurements

3.1 Physical Fundamentals

Before the space age our concept of the outer space around the Earth was a very simple one. Space was assumed to be essentially a vacuum, where matter only consisted of extremely high-energy particles originating from cosmic radiation. It was further believed that the magnetostatic fields stemming from electric currents in the interior of planets and stars were the only existing electromagnetic fields in space.

Since magnetic fields from celestial bodies decrease as the inverse third power to the radial distance no interaction took place among the bodies spanning our universe, and all magnetic distributions around planets, as Earth, had a structure similar to a dipole configuration.

Thus it was a major surprise when the first satellites orbiting the Earth observed a strongly perturbed Earth magnetic field and a large variability in the radiation and particle distribution around the outer tenuous part of the Earth's atmosphere.

The magnetosphere confined by the deformed Earth magnetic field is strongly influenced by the dynamic coupling with the interplanetary plasma, and therefore determined by the characteristics of the solar wind. The source for the solar wind is the sun's outermost region, the corona, which by convection and radiative transport processes establishes the particle content and magnetic relations of the solar wind.

These solar processes have large variations in time, energy and orientation. Through the means of the solar wind these processes also impinges on the structure and energy balance of the magnetosphere. The variations of the magnetosphere caused by the interaction with the solar wind are in turn also observed in the ionosphere, which constitute the upper ionized part of the atmosphere, tied by friction to the rotation of the Earth's neutral lower dense atmosphere.

The ionosphere is ionized mainly by the short wavelength part of the solar radiation (UV and soft X-ray) and to some extent also by particle precipitation. Thus this regions ionization state has large diurnal variations with maximum electron densities in the sunlit sector of the Earth. The strongest variations are monitored on the nightside of the Earth dominated by high energy particle fluxes from the tail of the Earth's magnetic field and magnetic field reconfiguration phenomena as substorm events.

Figure 3.1 shows the high latitude average electron concentration during a daytime and nighttime situation, respectively, for high and low solar activity. The regions of the lower ionosphere (E, F1, and F2) are clearly seen. They originate from the changes in the density and composition of the medium together with recombination processes related to the ionization caused by the solar radiation.

The F2 region is dominated by the atomic ion species O^+ , He^+ , and H^+ ionized by the UV solar radiation. While the E-region composition mostly consists of molecular ion

species as NO^+ and O_2^+ , generated by the Lyman β and X-ray solar radiation and collisions between electron, ions and neutral particles due to the more dense atmosphere in this altitude range.

3.2 Atmospheric Conditions

The ionosphere regions structure according to the field line orientation of the Earth magnetic field. For invariant magnetic latitudes less than around 75° the closed field lines confine the ionosphere. While for latitudes larger than 75° the field lines are open and reconnected to the passing magnetic field of the solar wind.

Some of the effects of this plasma structuring are major changes in the particle precipitation leading to the auroral regions, also associated with the intense upward and downward pair of field-aligned currents depositing major energy amounts in the lower ionosphere.

The polar cap potential drop and the connected current systems changes the convection flows in and around the auroral transition region. One of the disturbances most prominent of the auroral oval is the magnetic substorm, giving rise to intensification of the auroral activity and variations in the ionospheric electron density distribution together with major changes in the configuration of the nighttime convection cells.

The ionosphere conditions show also large latitudinal variations paired with seasonal changes. Figure 3.2 gives the daily observations of the peak electron density values for the E and the F2 region for high latitudes during summer and winter conditions. The left panel indicates the winter changes in the F region, giving rise to large gradients in the refractive index around the terminator of the sunlit ionosphere.

The tropical ionospheric effects arising from the equatorial electrodynamics lead to an enhanced electron density in the noon to afternoon sector local time. It occurs when an eastward ambient electric field is enhanced and thereby drifting the F-region plasma to higher altitudes, where the recombination is slower. After sunset a combination of pressure forces and gravity start to drift the plasma along the magnetic field, which is almost horizontal, to the tropical regions leading to enhanced plasma densities. This phenomenon is referred to as the equatorial anomaly.

The equatorial ionosphere has also major daily changes associated with the equatorial anomaly. Figure 3.3 shows in the upper panel the maximum F2 region electron density as function of the local time. While the lower panel reveal the latitudinal variations as function of altitude. The curves have been offset on the ordinate axis for better to be able to see the variations.

3.3 Electromagnetic Wave Propagation in the Atmosphere

The only way efficiently to observe the large ionosphere plasma region is by applying remote sensing techniques using electromagnetic radiation in the frequency domain from 1 MHz (MF and HF band.) to 39 GHz (SHF band). The propagation and energy flux relation of the waves for these wavelengths are to varying extent influenced by the natural frequencies of the plasma, characterizing the medium itself, as the plasmafrequency, gyrofrequency, collision frequencies and the scale sizes determining the plasma physical processes.

By combining information of the electromagnetic wave propagation direction and velocity, phase and amplitude changes, it is possible to monitor the characteristics of the dispersion relation governing the plasma.

In the ionosphere it is also related to the direction of the ambient magnetic field of the Earth and thereby the polarization of the wave probing the plasma. For planar high frequency electromagnetic waves the refractive relations can be described by the Appleton-Hartree formulation, which expresses the wave field dependence on the characteristic frequencies of the medium. The refractive index can be expressed as,

$$\mu^2 = 1 - \frac{X(U-X)}{U(U-X) - \frac{1}{2}Y^2 \sin^2 \zeta \pm \sqrt{\frac{1}{4}Y^4 \sin^4 \zeta + Y^2 \cos^2 \zeta (U-X)^2}} \quad U = 1 - iZ$$

where X, Y and Z are dimensionless quantities relating the wave frequency with the plasmafrequency, gyrofrequency and collision frequency, respectively. ζ defines the angle between the direction of the constant ambient magnetic field and the wave number vector.

For the neutral part of the atmosphere consisting of the troposphere and stratosphere the refractive relation is dominated by the wave polarization from the atmospheric molecules together with the permanent dipole moment of water molecules related to the moisture content of the air mass. The refractive relation for L-band waves in the lower atmosphere becomes,

$$\mu = 1 + k_1 \frac{P_d}{T} + k_2 \frac{P_w}{T^2} + k_3 \frac{P_w}{T}$$

where P_d is the partial pressure of the dry air mass, T the absolute temperature of the atmosphere, P_w the partial pressure of the water vapor content. k_i , ($i=1-3$) are constants of the neutral gas with evaluated values of the order of: $k_1 = 7,760 \cdot 10^{-5}$, $k_2 = 3,739 \cdot 10^{-1}$, and $k_3 = 7,040 \cdot 10^{-5}$.

4. Measurement Methods and Trade-off

4.1 Ionospheric Measurements

The ionosphere is the region of the atmosphere covering the altitude range from roughly 80 km to 1500 km. Even though the neutral density is larger than the ionized portion of the gas, the latter determines the processes describing the medium in union with the external forces and the particle precipitation originating from the magnetosphere, the solar wind and the Earth's magnetic field.

The formation of the ionosphere in layers or regions is a result of the interplay between the incident radiation and particle precipitation and the occurrence of different atom and molecular species in the upper atmosphere. The complicated structure resembles a set of Chapman electron density distributions for most conditions with the E and F regions as the dominating layers.

The maximum electron density of the ionosphere is normally attributed to the F2 region. The height of the peak electron density varies from about 250 km to 400 km. While the maximum electron density for the E-region cover altitudes from 100 km to 150 km.

The dispersive nature of the ionosphere plasma has a major impact on the electromagnetic wave characteristics and propagation. Thus the conditions in the ionosphere are important for the performance of all space-based communication, navigation, and surveillance systems.

To monitor the physical parameters of the atmosphere essential only two methods exist. They are,

1. In-situ measurements
2. Remote sensing observations

Each of these techniques has its own advantages and disadvantages, and usually observations from both are required to provide a comprehensive understanding of the ionosphere and its physical processes.

In-situ measurements give information on the local environment of the ionosphere normally limited in spatial extent by the gyroradius of the ion species of the plasma. Thus these observations reveal the small scale phenomena in the ionosphere.

Due to the spatial large scale of the ionosphere these observations alone tell very little about the processes leading to the observed local phenomena. Thus model results or other types of observations from space and ground often complement in-situ measurements.

In-situ measurements are destined to follow certain observational constraints, as the orbit of the satellite. Therefore they will not always monitor the physical processes in question and their development, which again leads to problems in separating spatial and temporal phenomena and conditions in the observations.

Remote sensing methods can be divided into, 1) backscatter and/or radar techniques and 2) transmitter-receiver observations of the integrated impact on the probing signal. Backscatter/radar methods give excellent observations of the atmosphere in local regions with higher coverage than in-situ measurements. The major drawback of the technique is that it normally requires high-power transmitter and large receiving antennas or antenna arrays. Thus most measurements of this kind are done from ground.

The transmitter-receiver integrated probing of the ionosphere has as one of its strong sides that it can cover large parts of the ionosphere leading to a comprehensive understanding of the physics taking place in the ionosphere. The GPSOS experiment is of this class. Since GPSOS uses an existing set of transmitters the cost of the mission is rather modest, which again leads to a possibility of a long-term monitoring of the ionosphere for space weather and climate activities.

Due to the large number of high precision transmitters in the total GPS and GLONASS system (up to 48) the number of low Earth orbiting (LEO) satellites only limits the spatial coverage.

It is possible with this technique to monitor the spatial and temporal development of the defined GPSOS observables, which consists of total electron content (TEC), slant-path TEC, electron density profiles, refractivity distribution, scintillations and their phase and amplitude spectra.

The major drawback of the technique is, that the observed parameters are integrated measurements through a medium, which sometimes at specific latitudes is highly variable. The small relative vertical extent of the ionosphere of the Earth compared to the radius of the Earth together with the radial structuring of the ionosphere lead to a highly detailed information vertically. This fact dissolves for a major part the intrinsic limitation of the technique.

Applying tomographical representation of the observations will result in further enhancements of the data products. Thus many LEO platforms performing GPSOS measurements can improve the precision in the description of the ionosphere conditions.

4.1.1 Scintillations

A radio wave traversing ionospheric irregularities consisting of unstable plasma waves or small-scale electron density gradients will experience phase and amplitude fluctuation. As long as the irregularities and the locations of transmitter and receiver do not change, a single receiver at a fixed location would detect a constant amplitude and phase.

Temporal or spatial changes of the irregularities as well as changes in the relative location of the transmitter/receiver system produce irregular temporal fluctuations of received signal amplitude, phase and direction of arrival of the signal. This is the definition and origin of scintillations. For the GPSOS observations the temporal changes of the ionospheric irregularities plays a minor role, since the transmitter/receiver location change dominates over the time scale of the natural changes in the plasma due to the irregularities.

The scintillations are predominantly observed in the F region of the ionosphere. But also E region irregularities, particularly sporadic E and auroral E, produce scintillations. The height range of the F regions, where irregularities are observed, range from 200 km to 1000 km at high latitudes, and between about 250 and 400 km at equatorial latitudes.

The usual measure of the strength of amplitude scintillation is the S_4 index. S_4 is defined as the root mean square of the variance of received power divided by the mean value of the received power. Phase scintillation strength is characterized by the standard deviation of the phase σ_ϕ over a given interval of fluctuation frequencies. For S_4 less than 0.6, the amplitude scintillation has a frequency dependence of approximately $f^{-1.5}$. Whereas σ_ϕ varies as f^{-1} for both weak and strong scintillation in the frequency range used by the GPS and GLONASS systems.

The morphology of amplitude scintillations emphasizes two essentially regions with high probability of intense scintillations at high and equatorial latitudes. Both bounded by magnetic and not geographic latitudes. For the high latitude region one has to use invariant latitudes or dipole latitudes for the representation. While for equatorial latitudes it is more appropriate to use dip latitudes. The most intense amplitude scintillations are to be expected for high solar activity in the region around the crests of the equatorial anomaly around the equinoxes and in the evening hours in the local time sector from 20 to 24 hours.

The observation of phase scintillation on a single GPS signal is difficult because of multipath problems, since stronger amplitude scintillations couple to phase scintillations with excursions of the L₁-L₂ phase. Up to 8 radians have been observed in phase scintillation. While amplitude fading can amount to 5 dB or more (a factor of two in amplitude) during strong solar activity. Figure 4.1 gives the global spatial variations in the amplitude fading during maximum and minimum solar activity conditions.

The strongest phase excursion reported on L₁-L₂ reached almost 14 radians during a period of 30 seconds. Based on earlier observations it is safe to assume, that a rate of phase change of L₁-L₂ higher than 1 Hz will not be the typical event. Applying the frequency law f^{-1} for phase scintillations gives for 10 Hz fluctuations peak-to-peak excursions less than 1 radian.

Power spectra of the upper ionosphere plasma density have been detected as well by in-situ measurements (rockets) and trans-ionospheric satellite measurements. The results show for both the auroral and equatorial electrojets a power law relation of the form k^n ,

where k is the wave number of the scintillations and n a number varying from 1.5 to 5 depending on the geomagnetic conditions, latitude and scale size of the irregularities.

A range of observations, simulations, and theoretical considerations indicate that for high k the spectral shape is determined by the Kolmogorov turbulence theory. This theory states, that due to the conditions for the unstable waves the plasma structures will form in the region of k space close to the natural scale sizes in the plasma. Figure 4.2 show a schematical representation of the scintillation spectrum including the dominant processes leading to the characteristics for the different regions in the spectrum. Energy cascades towards larger k values leading to a turbulence spectrum, which cease at a wave number, where energy dissipation occurs due to molecular viscosity. The turbulence theory indicate, that a more shallow spectral slope will be observed for wave numbers centered around $k \sim 30 \text{ m}^{-1}$ ($\lambda_0 \sim 0.2 \text{ m}$, $f \sim 1.5 \text{ GHz}$), where the GPSOS system operates. Figure 4.3 gives an observed power spectrum from a rocket experiment at lower latitudes.

4.1.2 Total Electron Content

One of the basic parameters of the GPSOS mission is the total electron content observation (TEC). It is defined as the integrated measure of the electron density along the path between two points. The ionosphere TEC defined as,

$$TEC = \int_{Path} N_e(s) ds$$

where $N_e(s)$ is the electron density along the propagation path between the source and the detector, can be split into 1) *vertical TEC*, normally given from the surface of the Earth and up, and 2) *slant-path TEC* defined by the total electron density along the ray path between transmitter and receiver at angles deviating from the radial direction with respect to the center of the Earth.

Measurements of TEC is crucial for the derivation of the secondary EDRs too, since it is part of the retrieval process of the neutral atmosphere parameters that a correction is done for the ionosphere contribution to the measured refractivity profile. But TEC is also a good measure of the spatial changes in the global electron density structures of the ionosphere. TEC acts as an indicator of geographical, seasonal, and diurnal variations in the ionosphere, resulting from the combined effects of solar radiation and transport processes of electrons and ions from one region to another.

Vertical TEC show large spatial changes especially at high latitudes in the auroral regions. The magnitude can here increase to several hundreds TEC units (1 TEC unit = 1 TECU = $10^{16} \text{ electrons/m}^2$). In the other region of particular interest, the equatorial region, TEC is often quite large amounting up to 400 TECU. The slant-path TEC may maximize during high sun spot periods at 1000 TECU. The reason for this is that the signal passes through the ionosphere two times from the transmitter (GPS/GLONASS satellite) and to the receiver on the LEO satellite (NPOESS satellite).

TEC has been studied for many years using Faraday rotation and differential Doppler techniques. These measurements provide important information about the ionosphere variability through the measurements of the temporal and spatial variation of TEC. Simultaneous TEC data have been used to study horizontal (latitudinal as well as longitudinal) variations of ionospheric structures.

Since TEC is the line integral of the electron density along the ray path, the information about the spatial variation of the electron density along the path caused by irregular structures cannot be recovered using the conventional procedure to process TEC data. Therefore ionospheric imaging is applied when having many TEC measurements of the ionosphere. This method has the capability of producing a two-dimensional picture of the ionospheric electron density distribution by using the one-dimensional TEC information.

Two different techniques are normally used when measuring ionospheric TEC. The first method relies on the differences of the P-code measurements from the L1 and L2 frequencies in order to generate the TEC observations. While the second method uses the differences between the probing carrier phases to generate the biased TEC measurements. The latter is more precise than the code based method. But the technique contains an unknown bias, arising from the ambiguity of the phase measurements governed by the unknown TEC above the satellite orbit. Normally both methods (code and phase measurements) are combined to generate a single TEC quantity. It is based on the precision of the phase measurement with the phase bias determined from either the code measurement or from a statistical optimized model of the upper part of ionosphere to the observed TEC profile.

The ionosphere as a dispersive medium leads to different phase delays as well as to different ray paths (bending) for the L1 and L2 frequencies. When passing through the ionosphere while approaching the closest distance to the surface of the Earth the L1 and L2 rays split and subsequently traverse the atmosphere at slightly different heights (up to one kilometer separation at the impact height is predicted during strong ionospheric disturbance conditions). After leaving the atmosphere and approaching the LEO the separated L1 and L2 rays are again subject to different bending.

The standard dual frequency range correction eliminates most of the ionospheric error by canceling the first order slant path TEC contribution, which would contribute to errors from the order of 1 m at nighttime to the order of 100 m at daytime during solar maximum conditions. However higher order effects (mainly the ray path splitting) lead to residual range errors up to the order of 10 cm. These, if uncorrected, prevent accurate retrieval of the secondary EDR atmospheric parameters.

Improved correction of the above technique is a difficult task. But since the actual bending depends on both the asymmetry of the inbound and outbound ionosphere and on the actual ionospheric layering during the occultation events it is possible to include this knowledge into the correction methods.

Bending angle correction technique instead of ranges is one of these techniques. This is a significant improvement to standard range corrections since it exploits the fact that most of the total bending is accumulated at grazing incidence near the ray perigee in the atmosphere.

Further theoretical studies show that also Doppler shift corrections instead of ranges or bending angles can nominally improve the accuracy of the achievable atmospheric parameters.

An approximation to the dispersion relation is used to retrieve the EDR products for TEC that requires no external data. The refractive index, defined as,

$$|\mu|^2 = 1 - \left[\frac{f_{plasma}}{f} \right]^2$$

where f_{plasma} is the plasmasfrequency of the electron gas in the ionosphere and f the probing electromagnetic wave frequency used by the GPS/GLONASS system, combines directly the electron density with the refractivity of the ionosphere plasma. This together with the relation for the excess phase change,

$$\Delta\Phi = \lambda^{-1} \left(\mu(s)ds - R_{LG} \right)$$

where R_{LG} is the line-of-sight distance between receiver and transmitter, λ the wavelength of the probing signal, and μ the refractive index along the ray path, turns out to be a very good approximation for most ionospheric conditions.

Applying the full refractive index expression (see chapter 3) requires external knowledge of the Earth's magnetic fields magnitude and configuration. To monitor the full impact of the terms including the magnetic field, knowledge is required of the Earth magnetic field that is to be better than the components stemming from dipole magnetic field.

In the retrievals of the GPSOS data products we plan to use the simpler approximation above by combining the whole set of $\Delta\Phi$ during an occultation to retrieve the variations in the refractive index.

Figure 4.4 shows an example of our retrieval software for TEC. The observations originate from the ‘Primetime 4’ period of the GPS/MET experiment. This specific occultation data set is from the time period, 22.20-22.30 UT, on 20th February 1997, at latitudes around 50° N during a rising occultation. The E and F2 region is clearly depicted in the retrieval.

The ray path of the GPS/GLONASS signal is bent due to the dispersive nature of the ionospheric plasma. The bending angle $\alpha(r)$ is closely linked to the Doppler shift of the received signal. For a spherically symmetric atmosphere, assuming a layered model of the ionosphere, the ray path can be estimated analytically. A unique relationship is de-

rived via the Abel integral transform between the bending angle $\alpha(r)$ and the refractive index $\mu(r)$ as function of the distance from the center of Earth. The integral equation derived for the above assumption becomes,

$$\mu(r) = \exp \left| \pi^{-1} \frac{\alpha(\xi)}{r \sqrt{\xi^2 - r^2}} d\xi \right|$$

where

$$r = \frac{a}{\mu}$$

$$\alpha = \Theta - \arccos\left(\frac{a}{R_L}\right) - \arccos\left(\frac{a}{R_G}\right)$$

$$\dot{L}_1 + \dot{R}_{LG} - (\dot{R}_L \cos\phi(a) - \dot{R}_G \cos\chi(a)) = 0$$

Figure 4.5 gives for the same data set as in Figure 4.4 the bending angle profile under the described above assumptions. The bending angles at the highest altitudes show large variations due to the low phase change and the ambiguity describe above. The angles are defined in figure 5.1

4.1.3 Ionospheric Refractivity

The magnitude of refractivity N (defined as $N = (\mu-1) \cdot 10^6$) is in the ionosphere slightly negative having value of around from -10 to -50 for the GPS/GLONASS frequency range. In the troposphere of the neutral atmosphere refractivity increase to values from 100 to 500 leading to a major increase in the excess phase compared to the values observed in the ionosphere. Thus it is valuable to have the refractivity profile in the ionosphere to determine the errors in the retrieval of the other EDRs.

Furthermore ionospheric refractivity plays a role in all derivations of EDRs for the ionosphere as well as for the stratosphere and troposphere. The errors in the refractivity profile are much smaller than the errors coming from the bending angles assuming spherical symmetry. Thus having additional information on the ray path of the probing waves lead to a highly precise estimate of the electron density profile.

4.1.4 Electron Density

The electron density profile at the lowest impact height of the ionosphere gives a good measure of the characteristics of the layers in the ionosphere together with magnitudes and altitudes of the maximum electron densities.

The retrieval technique planned for the retrieval of this EDR follows the following steps.

- Observations of the phase delays for L1 and L2
- Calculation of TEC
- Calculation of the bending angle profile
- Inversion of bending angles using the Abel transform
- Retrieval of the electron density profile

The input data are the precise positions and velocities of the two satellites performing the observation (GPS/GLONASS satellite and GPSOS LEO satellite) together with the phase delay of the two frequencies L1 and L2. Only carrier phases are used.

TEC along the ray path through the ionosphere is calculated. TEC is obtained from the difference of the L1 and L2 phase delays. This is done to have correlated clock errors cancel out. The phase delays and thus the bending caused by the ionosphere are very small. The ray path of the occulted radio beam can therefore be assumed to be close to a straight line. With this assumption the phase delay can be calculated from the TEC.

$$L_1 = \underset{\text{ray path}}{\int} \left(1 - C \frac{N_e}{f_1^2} \right) ds - R_{LG} = \frac{-C}{f_1^2} TEC = \frac{-f_2^2}{f_1^2 - f_2^2} [L_1 - L_2]$$

$$TEC = \frac{f_1^2 f_2^2}{C(f_1^2 - f_2^2)} [L_1 - L_2]$$

C is a constant of the ionosphere ($C = 40.3 \text{ m}^3 \text{ s}^{-2}$) and f_1 and f_2 are the two probing frequencies. N_e is the electron density along the ray path and R_{LG} is the straight line distance between the GPS and the LEO satellite.

From the phase delay obtained this way, i.e. without clock errors, the bending angle as a function of impact parameter is calculated. This involves a differentiation of the phase with respect to time. Thus the sampling rate needs to be sufficiently high, preferable 1 Hz or higher.

At high impact parameters the calculated bending angle is fitted by an exponential expression in order to eliminate errors introduced near the height of the LEO orbit. For the GPS/MET satellite observations we have used an exponential optimized fit of impact parameters between 550 km to 650 km. This exponential fit is needed when calculating the refractive index using the Abel transform since the integral goes to infinity.

Under the assumption that the electron density is spherically symmetric the refractive index $\mu(a)$ and the electron density can be obtained from the bending angles $\alpha(a)$ using the Abel transform.

$$\ln(\mu(a)) = \frac{1}{\pi} \int_a^{\infty} \frac{\alpha(\xi)}{\sqrt{\xi^2 - a^2}} d\xi$$

The electron density is finally obtained using the expression for the refractive index in the ionosphere to the first order. Effects originating from solar activity and the higher order terms from the magnetic field are neglected.

$$N_e(a) = \frac{(1 - \mu(a)) f_1^2}{C}$$

When the assumption of spherical symmetry is violated the electron density calculated in this way can become negative. This is of course not real, but simply reflects, that horizontal data from for example tomography would be needed to construct the true electron density profile.

This procedure to calculate electron density profiles does not rely on an absolute determination of the TEC. The bending angle profile is obtained by differentiating the observed phases. So only the shape of phase profile is important.

The absolute value of the horizontal TEC can be determined fitting an exponential function at high impact parameters and subtract the offset. However the near zenith TEC must be determined by other means, i.e. calculating TEC using code phase information as earlier described.

The algorithms described above have been tested on model data generated by a forward ray propagation simulator together with global models of the disturbed ionosphere. Comparing the electron density profile obtained using the Abel transform with the ‘true’ electron density from the input model ionosphere a near perfect match is obtained.

Figure 4.6 show the relative differences between the input electron density profile, applying Chapman layers for the E and F2 region, and the resulting retrieved electron density profile. The solid curve represents the inversion scheme, where the phase delay has been calculated from the L1-L2 difference as given above, thereby eliminating the clock errors in the measurement. The dashed curve represents the relative difference when using only using L1 and no clock errors. From the curves it is evident, that the relative difference is less than 1% near the peaks of the electron density profiles.

A small bias may be introduced at high impact parameters when the bending angles are fitted to an exponential expression. By subtracting this bias the errors reduce to below 0.5% for all heights.

Figure 4.7 show the simulation results of the electron density errors of the retrieval technique when applying 1mm uncorrelated Gaussian noise to both probing frequencies, L1 and L2, and applying the developed algorithms for the electron density retrieval described above. The experiment shows only minor errors between the undisturbed profile (dotted line) and the profile with the phase noises included (full line).

The algorithms have also been applied to ionosphere observations from the GPS/MET satellite. Figure 4.8 gives the estimated electron density profile from an GPS/MET occultation observation. Both the E and F2 region and their characteristics are clearly identified in the retrieval.

4.2 Neutral Atmospheric Measurements

The atmospheric profiling technique provides measurements of the Doppler shift of the probing GPS/GLONASS signals that have passed through the limb of the atmosphere. The magnitude of the shift is related to the atmosphere's refractivity gradients along the path of the signal. These in turn are related to the neutral atmosphere's temperature, pressure and humidity fields.

Provided that the signal has sufficiently high quality (i.e. signal-to-noise ratio) and that other variables of the experiment (e.g. the positions of the transmitter and receiver, and the effects of the ionosphere) are known to sufficient accuracy, information on the temperature and humidity fields can be retrieved. More specifically, from series of measurements obtained during the occultation event, the profiles of temperature and humidity close to the tangent point of the signal path can be estimated.

The secondary EDRs relating to the stratosphere and troposphere retrievals are setting the highest demands on the accuracy of the observables and the Precise Orbit Determination (POD) estimates. To comply with these requirements the software algorithms follows two routes for determining the dry state of the lower neutral atmosphere and the water vapor profile of the troposphere.

The occultation technique is defined by the geometry, where the transmitter and the receiver are positioned relative to the Earth in such an arrangement, that the radio wave signal traverses the atmosphere from the ionosphere to the limb of the Earth and back again towards the LEO satellite. The propagation path of the GPS/GLONASS electromagnetic wave through the atmosphere will be influenced by the dispersive characteristics of the medium, due to ionized and neutral part of the gas of the atmosphere. Ray bending and changes in the phase and amplitude of the transmitted signals, caused by the conditions in the ionosphere and troposphere/stratosphere, are the results.

The dispersion relation for the electromagnetic wave probing the atmosphere can be defined as the real part of the refractive index μ , when discarding the absorption of the wave in the media. The total atmosphere refraction can be approximated to the relation:

$$N = k_1 \frac{P_d}{T} + k_2 \frac{P_w}{T^2} + k_3 \frac{P_w}{T}$$

where $N = (\mu - 1) \cdot 10^6$, P_d is the partial pressure of the dry air mass (in hPa), T the absolute temperature of the atmosphere (in Kelvin), P_w the partial pressure of the water vapor content (in hPa). $k_{i,(i=1-4)}$ is constant of the neutral gas with evaluated magnitudes of, $k_1 = 77,60$; $k_2 = 37,39 \cdot 10^4$; $k_3 = 70,40$.

The first term on the right-hand-side of the above equation is due to the dry part of the atmosphere, and is caused by the wave polarization of the molecules in the lower neutral atmosphere (troposphere and stratosphere). The second and third term relate to the moist atmosphere relation from the permanent dipole moment of water molecules. All these terms are independent of frequency. It is assumed that the ionosphere contribution can be estimated and removed, so that N only carries the neutral atmosphere contributions.

The moist terms have only a substantial impact on the magnitude of N in altitudes below 5 kilometer. Above altitudes of 7-10 kilometers the contribution to N from the water vapor terms is less than 2%. In the tropics the influence of water vapor has to be considered in the retrieval of the lowest part of the troposphere temperature profile. Thus, observations of refractivity itself is a measure of the combined effect of temperature and water vapor, and may ultimately be applied to weather and climate models as a consistent physical parameter describing the state of the atmosphere.

Taking account of the above considerations, N can be reduced to a function of only the dry term in the equation of refractivity. Combining this with the equation of state,

$$P = \frac{\rho RT}{m}$$

results in a directly proportional relation between the air mass density ρ and N . In other words, $\rho(r)$ can be obtained from the values of the refractive index. Applying hydrostatic equilibrium,

$$dP = -g\rho dr$$

where g represents the acceleration of gravity, establishes a relation between the pressure $P(r)$, at a certain height and the air mass density $\rho(r)$. The temperature $T(r)$ can now be obtained from $P(r)$ and $\rho(r)$.

In summary, vertical profiles of ρ , P , and T can be derived directly from the observed refractive index profile $\mu(r)$. The basic parts of this retrieval procedure, which is used in the developed software packages, can be synthesized as below.

Observables:	$L = \underset{\text{ray path}}{nd s} - R_{LG}$	L_1 and L_2
↓		
Ionosphere correction:	$L_C = \frac{f_1^2 L_1 - f_2^2 L_2}{f_1^2 - f_2^2}$	L_C
↓		
Neutral Doppler shift:	$\frac{dL_C}{dt}$	\dot{L}_C
↓		
Impact height:	$F(a) = \dot{L}_C + \dot{R}_{LG} - (\dot{R}_L \cos\phi(a) - \dot{R}_G \cos\chi(a)) = 0$	a
↑		
Bending angle:	$\alpha = \Theta - \arccos\left(\frac{a}{R_L}\right) - \arccos\left(\frac{a}{R_G}\right)$	$\alpha(a)$
↓		
Abel transform:	$\ln(\mu) = \frac{1}{\pi} \int_a^\infty \frac{\alpha(\xi)d\xi}{\sqrt{\xi^2 - a^2}}, \quad r = \frac{a}{\mu}$	$n(r)$
↓		
Neutral density:	$\rho = \frac{1}{k_1 R} \left(N - \frac{k_2 P_w + k_3 T P_w}{T^2} \right), \quad N = (\mu - 1) \cdot 10^6$	$\rho(r)$
↓		
Hydrostatic equation:	$P = \int_{R_E+z}^\infty \rho(r)g(r)dr$	$P(z)$
↓		
Equation of state:	$T = \frac{P}{R\rho}$	$T(z)$

4.2.1 Neutral Atmospheric Refractivity

The refractivity measurements is limited by the thermal noise for altitudes above 30 km. While horizontal variations in the refractivity limits the accuracy of the measurements for altitudes less than 25 km. The error in the refractivity profile is less than 0.4% for altitudes between 5 km and 30 km. Due to the nonlinear characteristics of the water vapor and its spatial distribution in the lowest altitudes of the troposphere closest to the surface of the Earth, refractivity here suffers from a increasing larger fluctuations, leading higher uncertainties of the refractivity profile in the boundary layer. The refractivity profile is determined as given above using the Abel transform and the ionosphere correction formed by the L1-L2 algorithm.

4.2.2 Temperature Profiles

Figure 4.9 and 4.10 are examples of the possible accuracies in the temperature profiles for the stratosphere and troposphere when retrieving the profiles using the above algorithms.

The profiles are also compared with the Fresnel transform having a higher vertical resolution than the Abel transform. But because of the long computation time for this retrieval method we suggest to apply the above described inversion scheme.

4.2.3 Moisture Profiles

In the altitude range varying from 5 km to 8 km in the troposphere the water vapor term in the refractivity equation can amount up to 30% of the total refractivity. Especially in the tropics this term can locally dominate the vertical refractivity gradients and bending near the surface of the Earth.

The recovery of the water vapor profile from the measurements of the refractivity N can be estimated from the below expression.

$$P_w = \frac{NT^2 - k_1 PT}{k_2}$$

The determination of P_w requires knowledge of the temperature profile derived from either climatological models, independent observations or from data fields from numerical weather prediction models. Since the vertical scale sizes of water vapor variability is much smaller than for the dry atmosphere, this may be used to constrain the wet and the dry contributions to the refractivity profile. Here a method is suggested, that assumes initially the profile of the temperature and then iteratively derive the pressure profile and the water vapor profile.

4.2.4 Pressure Profiles

The pressure profile is due the processes in the atmosphere and the scale sizes in the troposphere well defined throughout the lower neutral atmosphere. Thus the pressure profile exerts very small higher order vertical changes. This leads to a possibility to determine the pressure profile by having an initial guess of the temperature high in the atmosphere. Initial pressure errors in the temperature guess decrease rapidly as the integration moves deeper into the troposphere. The presence of significant amount of water vapor complicates the retrieval and the interpretation of the refractivity. However, in the

colder tropospheric regions where the water vapor plays a minor role, accurate profiles of the pressure can be retrieved with a high level of accuracy with the above algorithms.

5. Algorithm Description

5.1 On board algorithms

Scintillation indices and power spectra of the phase and amplitude variations are calculated internally in the GPSOS receiver to monitor the upper ionosphere plasma density fluctuations.

5.1.1 Amplitude Scintillations

5.1.1.1 Input data

The amplitude scintillation algorithm needs as input:

1. An array of measured power P samples for each frequency.
2. The time interval over which the average values are calculated.
3. The number of samples used in the measurement.

5.1.1.2 Output data

The amplitude scintillation algorithm gives as output:

1. The scintillation index S_4 .

5.1.1.3 Algorithm

The strength of amplitude scintillation is given by the S_4 index, defined as the root mean square of the variance of received power P divided by the mean value of the received power P .

$$S_{4i}^2 = \frac{\overline{P_i^2} - \overline{P_i}^2}{\overline{P_i}^2}$$

The suffix i indicates that the corresponding parameter can be evaluated for the two carrier frequencies f_1 and f_2 .

5.1.2 Phase Scintillations

5.1.2.1 Input data

The phase scintillation algorithm needs as input:

1. An array of measured samples of the signal phase S .
2. The time interval over which the average values are calculated.
3. The number of samples used in the measurement.

5.1.2.2 Ouput data

The phase scintillation algorithm gives as output:

1. The scintillation strength σ_ϕ .

5.1.2.3 Algorithm

Phase scintillation strength σ_ϕ is characterized by the standard deviation of the phase over a given interval of fluctuation frequencies. The bracket symbol $\langle \rangle$ indicate the mean value over some finite time interval, given by the number of samples and the time between two samples.

$$\sigma_{\phi i} = \sqrt{\langle S_i^2 \rangle - \langle S_i \rangle^2}$$

The suffix i indicates that the corresponding parameter can be evaluated for the two carrier frequencies f_1 and f_2 .

5.1.3 Spectral Scintillation Processing

5.1.3.1 Input data

The spectral scintillation algorithm needs as input:

1. An array of measured samples of the signal power P (and phase S).
2. The time interval over which the average values are calculated.
3. The number of samples used in the measurement.

□

5.1.3.2 Output data

The spectral scintillation algorithm gives as output:

1. An array of spectral estimator samples.

□

□

5.1.3.3 Algorithm

A spectral estimator for the scintillations can be found from the Wiener-Kinchine theorem. It states that the Fourier transform of the autocovariances function $C(\tau)$ is an estimator for the spectrum. The autocovariances function can then be found from the following equation

$$C(\tau) = \langle (P(t) - \langle P \rangle)(P(t + \tau) - \langle P \rangle) \rangle$$

□

Where t and τ represents time and time lag. A spectral estimator S_{pp} for the scintillation spectrum is then found from the Fourier transform below

$$S_{pp} = \frac{1}{T} \int_{-\infty}^{\infty} C(\tau) e^{-j2\pi f\tau} d\tau$$

The spectral estimator can also be found using the direct method where

$$S_{pp} = \frac{2\pi}{T} |U_{oT}|^2$$

and

$$U_{oT} = \frac{1}{2\pi} \int_0^T (P(t) - \langle P \rangle) e^{-j2\pi f t} dt = \frac{1}{2\pi} \sum_i (P(t_i) - \langle P \rangle) e^{-j2\pi f t_i} \Delta t_i$$

so

$$S_{pp} = \frac{1}{2\pi T} \left| \sum_i (P(t_i) - \langle P \rangle) e^{-j2\pi f t_i} \Delta t_i \right|^2$$

T is the measurement time interval, U_{oT} is the complex Fourier coefficient and Δt is the time between samples.

□

5.2 Post processing Algorithms

5.2.1 Total Electron Content

□

5.2.1.1 Input data

The Total Electron Content (TEC) is calculated using the following parameters as input:

- 1 The two carrier frequencies f_1 and f_2
- 2 The carrier phases L_1 and L_2
- 3 The two code phases P_1 and P_2 (pseudo range) to determine the phase ambiguity.

□

5.2.1.2 Ouput data

□

The output of the algorithm will be:

- 1 The total electron content measured in TEC units
(1 TEC unit = 10^{16} elec/m²)

5.2.1.3 Algorithm

Dual frequency slant TEC measurements are defined by the simple refractive index relation mentioned in chapter 4. This leads to the following relation for TEC,

$$TEC = \frac{f_1^2 f_2^2 (L_1 - L_2)}{C(f_1^2 - f_2^2)}$$

where C equals $40.3 \text{ m}^3 \text{ s}^{-2}$. To determine the absolute value of TEC it is necessary to solve for the phase ambiguity using the equations from section 7.2. f_i are the carrier frequencies for the L1 and L2 waves, respectively. The corresponding TEC calculated using the code phases is calculated using the same expression. Then the absolute value of the carrier phase TEC can be obtained by fitting, this determines the phase ambiguity bias.

5.2.2 Ionospheric Refractivity Retrieval

5.2.2.1 Input data

The ionospheric refractivity N is calculated using as input:

- 1 The precise position and velocity of both the LEO and the GNSS satellite \bar{R}_L , $\dot{\bar{R}}_L$ and \bar{R}_G , $\dot{\bar{R}}_G$ as array's of time.
- 2 The two carrier phases L_1 and L_2
- 3 The carrier frequencies f_1 and f_2
- 4 The sampling rate.

5.2.2.2 Output data

The output of the algorithm will be:

- 1 The ionospheric refractivity $N(h)$ as a function of height h .

5.2.2.3 Algorithm

The algorithm first determine the bending angle of L_1 using the following equations.

$$L_1 \approx \frac{-f_2^2}{f_1^2 - f_2^2} (L_1 - L_2)$$

where we have assumed that the ray path is a straight line. For each data sample the impact parameter a is found by solving the equations below

$$\begin{aligned} \dot{L}_1 + \dot{R}_{LG} - \left(\mu_i(\bar{R}_L) \left| \dot{\bar{R}}_L \right| \cos \varphi(a) - \left| \dot{\bar{R}}_G \right| \cos \chi(a) \right) &= 0 \\ \varphi(a) = \zeta - \arcsin\left(\frac{a}{|\bar{R}_L|}\right) \quad , \quad \chi(a) = (\pi - \eta) - \arcsin\left(\frac{a}{|\bar{R}_G|}\right) \end{aligned}$$

where η is the angle between position and velocity of the GPS satellite, ζ is the angle between position and velocity of the LEO satellite, ϕ is the angle between incoming ray and the velocity of the LEO satellite, χ is the angle between outgoing ray and the velocity of the GPS satellite. See figure 5.1. The bending angle α_i can now be found using

$$\alpha_i = \Theta - \arccos\left(\frac{a}{|\bar{R}_L|}\right) - \arccos\left(\frac{a}{|\bar{R}_G|}\right)$$

where Θ is the angle between the two position vectors. The ionospheric index of refraction μ can be found from the Abel transform.

$$\mu_i(a) = \exp\left(\frac{1}{\pi} \int_a^\infty \frac{\alpha_i(x) dx}{\sqrt{x^2 - a^2}}\right)$$

The refractivity N as a function of height h can be found by combining the following equations.

$$N = (\mu_i - 1)10^6, \quad h = \frac{a}{\mu_i(a)} - R_{curve}$$

where R_{curve} is the curvature radius of the earth at the tangent point.

5.2.3 Neutral Atmospheric Refractivity Retrieval

5.2.3.1 Input data

The atmospheric refractivity N is calculated using as input:

1. The precise position and velocity of both the LEO and the GNSS satellite
 \bar{R}_L , \bar{R}_G and $\dot{\bar{R}}_L$, $\dot{\bar{R}}_G$ as array's of time.
2. The two carrier phases L_1 and L_2
3. The carrier frequencies f_1 and f_2
4. The sampling rate.

5.2.3.2 Ouput data

The output of the algorithm will be:

1. The atmospheric refractivity $N(h)$ as a function of height h .

5.2.3.3 Algorithm

For each data sample the impact parameter a is found by solving the equations below

$$\dot{L}_i + \dot{R}_{LG} - \left(\mu_i(\bar{R}_L) \left| \dot{\bar{R}}_L \right| \cos \varphi(a) - \left| \dot{\bar{R}}_G \right| \cos \chi(a) \right) = 0$$

$$\varphi(a) = \zeta - \arcsin\left(\frac{a}{|\bar{R}_L|}\right) \quad , \quad \chi(a) = (\pi - \eta) - \arcsin\left(\frac{a}{|\bar{R}_G|}\right)$$

where η is the angle between position and velocity of the GPS satellite, ζ is the angle between position and velocity of the LEO satellite, φ is the angle between incoming ray and the velocity of the LEO satellite, χ is the angle between outgoing ray and the velocity of the GPS satellite. See figure 5.1. The bending angle α can now be found using

$$\alpha_i = \Theta - \arccos\left(\frac{a}{|\bar{R}_L|}\right) - \arccos\left(\frac{a}{|\bar{R}_G|}\right)$$

where Θ is the angle between the two position vectors and $i=1,2$ representing the two frequencies. The ionospheric corrected bending angle is found from the equation below

$$\alpha(a) = \frac{f_1^2 \alpha_1(a) - f_2^2 \alpha_2(a)}{f_1^2 - f_2^2}$$

The atmospheric index of refraction μ can be found from the Abel transform.

$$\mu(a) = \exp\left(\frac{1}{\pi} \int_a^\infty \frac{\alpha(x) dx}{\sqrt{x^2 - a^2}}\right)$$

The refractivity N as a function of height h can be found by combining the following equations.

$$N = (\mu - 1)10^6, \quad h = \frac{a}{\mu(a)} - R_{curve}$$

Where R_{curve} is the curvature radius of the earth at the tangent point.

5.2.4 Electron Density Retrieval

5.2.4.1 Input data

The electron density algorithm needs the following input:

1. The ionospheric index of refraction $\mu_i(h)$ as a function of height h .
2. The carrier frequency f_1 .

5.2.4.2 Ouput data

The output of the algorithm will be:

1. The electron density profile $N_e(h)$ as a function of height h .

5.2.4.3 Algorithm

The electron density profile N_e can be found from the ionospheric index of refraction using.

$$N_e(h) = \frac{f_1^2}{40.3082} (1 - \mu_i(h))$$

5.2.5 Temperature, Pressure and Moisture Profile Retrieval

5.2.5.1 Input data

TBD

5.2.5.2 Ouput data

TBD

5.2.5.3 Algorithm

The secondary EDR parameters of the neutral atmosphere consist of estimates of the temperature, pressure and moisture profile. The retrieval is based on the calculated refractive index profile given above.

$$P_{dry}(z) = \int_z^{\infty} \frac{N(z') g(z')}{2.22759 \cdot 10^4} dz'$$

$$T_{dry}(z) = \frac{77.60 P_{dry}(z)}{N(z)}$$

$$T_v(z) = T(z)(1 + 0.608q(z))$$

$$P(z) = P_{dry}(z_0) \exp\left(\int_z^{z_0} \frac{g(z')}{287.06 T_v(z')} dz'\right)$$

$$P_w(z) = T(z) \frac{T(z)N(z) - 77.60P(z)}{3.73 \cdot 10^5}$$

$$q(z) = 0.622 \frac{P_w(z)}{P(z)}$$

$P(z)$ and $P_w(z)$ are solved simultaneously by iteration below the altitude $z = z_0$. Above z_0 , the following relations apply $P = P_{dry}$, $T = T_{dry}$, and $P_w = 0$.

5.2.6 Precipitable Water Retrieval

5.2.6.1 Input data

The precipitable water algorithms need as input:

1. The refractivity profile N_w from the occultation related to the wet terms.
2. The profiles for temperature T and water vapor pressure P_w .

5.2.6.2 Output data

The below relations give as output:

1. Precipitable water PW.

5.2.6.3 Algorithm

A secondary EDR, which may be provided from the GPSOS system, is the calculated precipitable water defined from the water vapor profile of the troposphere. In general the GPSOS system is not sensitive to rain or snow particles in the lower troposphere. This is due to the wavelength of the transmitted signals compared to the scale sizes of the particles and the geometry of the observation having the transmitters far away from the probed medium and the receiver. But precipitable water (PW) may also be interpreted as the vertically integrated water vapor at a position on ground, where the water vapor profile from the occultation has its footprint at the surface of the Earth.

From the occultation measurements the wet delay of the refractivity can be mapped onto PW. This is normally calculated at ground GPS sites to monitor the delay caused by the integrated water vapor during a GPS satellite pass over the receiving station.

In other words PW is the integrated water vapor profile mapped onto the precipitable water (Bevis et al., 1994). The following relations define the mapping function for PW in relation to the zenith wet delay ZWD.

$$PW = \Pi \cdot ZWD$$

$$\Pi = (\rho R_w (k_2 \cdot T_m^{-1} + (k_3 - m \cdot k_1))) \cdot 10^{-6})^{-1}$$

where ρ is the density of liquid water, R_w the specific gas constant for water vapor, $m=M_w/M_d$ the ratio between the molar mass of water vapor and dry air, and $k_{i=1,3}$ the constants of the neutral gas given in the expression for the refractivity N of the medium (see chapter 4). With these constants of the neutral atmosphere the last equation defines Π as function of T_m , which is given as the weighted mean temperature of the atmosphere.

$$T_m = \frac{\frac{P_w}{T} dz}{\frac{P_w}{T^2} dz}$$

In the last equation P_w represents the water vapor pressure and T the temperature of the troposphere.

6. System Error Analysis

6.1 Definition of Atmospheric Conditions

Atmospheric profiling observations based on GPS/GLONASS occultation measurements give an excellent description of a range of parameters in the ionosphere and the stratosphere/troposphere in the lower neutral atmosphere. The total observational system introduces different errors and biases to the retrieved data products. The error sources originate from the GPSOS sensor on the LEO, the GPS and GLONASS transmitting satellites, the medium, and the applied data retrieval theories and developed algorithms. All elements of the system contribute to a complex picture of the error sources and the sensitivity of the system.

To identify and quantify the different errors, accuracies and uncertainties of the different parts of the system a set of scenarios for the ionosphere and the troposphere have been chosen for further simulations. They will all present cases of *the best*, *the nominal* and *the worst case conditions* in the atmosphere to test the capabilities of the technique.

These simulations will be performed using the software tool EGOPS and routines developed specifically for this purpose at DMI to monitor the sensitivity and impact of phenomena in the ionized upper atmosphere (ionosphere) and the lower dense neutral atmosphere (stratosphere/troposphere).

6.1.1 Ionosphere scenarios

These scenarios will describe ionosphere conditions driven by structures in the electron density distribution in order to observe the predicted ‘truth’ in the estimated EDR observables. Furthermore these scenarios will demonstrate the influence of external forces originating from the sun on the ionosphere estimates. Two scenarios will center on the conditions in the auroral region as well as the phenomena in the equatorial electrojet.

The simulated scenarios cover the conditions,

- Auroral region electron density gradients
- Equatorial electrojet phenomena
- Electron density variations as function of day-night time terminator conditions
- Travelling Ionospheric Disturbances (TID)

- Ionosphere high gradient disturbances in the 3D global electron density distribution

6.1.2 Stratosphere/Troposphere scenarios

These scenarios cover conditions in the atmosphere leading to large gradients in the global spatial refractive index of the medium. Additionally dynamical wave activity, which may cause multi-path phenomena, will be simulated and tested.

The scenarios are,

- Troposphere frontal systems
- Tropopause foldings
- Troposphere inversion layer conditions
- Gravity waves

6.2 Algorithm error assessment

We will in this section perform an assessment on the errors associated with measurements based on the occultation principle. In order to make this error analysis thorough, the accuracies and uncertainties on the measured physical parameters are based on figures from the literature and simulations with the simulation program EGOPS. Equations for the accuracy and uncertainty on some of the physical parameters have also been derived. The simulation results are based on the current state of the algorithms under development and does not necessarily represent final performance. Areas where improvements are expected are indicated below.

The measurement *accuracy* is defined as the difference between the mean estimated value of a parameter and its true value, while the measurement *uncertainty* is defined as the root-mean-square of the measurement errors for the estimated parameter.

6.2.1 Slant Total Electron Content (Slant TEC)

In this section the accuracy and uncertainty on the calculation of the slant total electron content will be found. Equations for the carrier phase L and code phase P has been given in an earlier section. In equation (1.1.1) and (1.1.2) the index of refraction in the ionosphere has been expressed in a power series expansion that includes terms up to the second order. The effect of the neutral atmosphere has been neglected, since we assume a measurement for which the tangent point is above 100 km.

\hat{L} and \hat{P} are the measured carrier and code phases, including phase ambiguities and clock errors, while L and P gives the theoretical expressions for carrier and code phases

$$\begin{aligned} L_1 &= \int_1 C \frac{N_e}{f_1^2} - K \frac{N_e B_0 \cos(\theta)}{f_1^3} ds - R_{LG} \\ \hat{L}_1 &= L_1 + \Delta\beta_{L1} - B_1 + \varepsilon_1 \\ L_2 &= \int_2 C \frac{N_e}{f_2^2} - K \frac{N_e B_0 \cos(\theta)}{f_2^3} ds - R_{LG} \\ \hat{L}_2 &= L_2 + \Delta\beta_{L2} - B_2 + \varepsilon_2 \end{aligned} \tag{1.1.1}$$

$$\begin{aligned}
P_1 &= \int_1^2 C \frac{N_e}{f_1^2} + 2K \frac{N_e B_0 \cos(\theta)}{f_1^3} ds - R_{LG} \\
\hat{P}_1 &= P_1 + \Delta\beta_{P1} + \varepsilon_{gr1} \\
P_2 &= \int_2^3 C \frac{N_e}{f_2^2} + 2K \frac{N_e B_0 \cos(\theta)}{f_2^3} ds - R_{LG} \\
\hat{P}_2 &= P_2 + \Delta\beta_{P2} + \varepsilon_{gr2}
\end{aligned} \tag{1.1.2}$$

where

$$\begin{aligned}
C &= \frac{1}{2} e^2 / 4\pi^2 m \varepsilon_0 \approx 40.3 \text{ m}^3 \text{s}^{-2} \\
K &= \frac{1}{2} e^3 / 8\pi^3 m^2 \varepsilon_0 \approx 1.1283 * 10^{12} \frac{\text{C}}{\text{kg}} \text{m}^3 \text{s}^{-2}
\end{aligned} \tag{1.1.3}$$

$\Delta\beta$ is an error term caused by the difference in the GPS and LEO clocks. B is the phase ambiguity bias, while ε and ε_{gr} are the random errors for the carrier phase L and the code phase P . These random errors are generated in the receiver electronics on board the LEO satellite. N_e is the number density of electrons, and B_0 is the magnitude of the earth's magnetic field. θ is the angle between the directions of the ray and the magnetic field. In general we have that the random error for the code phase is larger than the corresponding error for the carrier phase, $\varepsilon_{gr} > \varepsilon$. We have in the equations for the code phases neglected a bias term assuming that this bias type has been corrected. Suffix 1 and 2 in the line integrals represent the paths followed by the two radio waves between the GPS and LEO satellite. Suffix 0 represents the straight line between the two satellites.

The phase ambiguity for the carrier and code phase can for an ensemble of measurements be determined by the following equation

$$\hat{B}_L = \frac{\sum_i w_i (\hat{L}_1 - \hat{L}_2 + \hat{P}_1 - \hat{P}_2)_i}{\sum_i w_i} = \frac{\sum_i w_i B_L^i}{\sum_i w_i} \tag{1.1.3}$$

where w_i is a SNR based weight factor.

From (1.1.1) and (1.1.2) we have

$$\begin{aligned} (\hat{L}_1 - \hat{L}_2 + \hat{P}_1 - \hat{P}_2) &= (B_2 - B_1) + 2(\hat{L}_1 ds - \hat{L}_2 ds) + (\Delta\beta_{L1} - \Delta\beta_{L2}) + (\Delta\beta_{P1} - \Delta\beta_{P2}) \\ &+ \left(K \frac{N_e B_0 \cos(\theta)}{f_1^3} \right) ds - \left(K \frac{N_e B_0 \cos(\theta)}{f_2^3} \right) ds + \epsilon_1 - \epsilon_2 + \epsilon_{gr1} - \epsilon_{gr2} \end{aligned} \quad (1.1.4)$$

So

$$B_L^i = (B_2 - B_1)_i + \beta_B^i + \epsilon_1 - \epsilon_2 + \epsilon_{gr1} - \epsilon_{gr2} \quad (1.1.5)$$

where

$$\beta_B^i = 2(\hat{L}_1 ds - \hat{L}_2 ds)_i + (\Delta\beta_{L1} - \Delta\beta_{L2})_i + (\Delta\beta_{P1} - \Delta\beta_{P2})_i + \left(K \frac{N_e B_0 \cos(\theta)}{f_1^3} \right) ds - \left(K \frac{N_e B_0 \cos(\theta)}{f_2^3} \right) ds \quad (1.1.6)$$

And then

$$\beta_B = \frac{\sum_i w_i \beta_B^i}{\sum_i w_i} \quad (1.1.7)$$

so the phase ambiguity

$$\hat{B}_L = B_2 - B_1 + \beta_B \quad (1.1.8)$$

from equation (1.1.3) can be found and β_B is then a measure for the accuracy on the phase ambiguity term \hat{B}_L .

Since the dominating uncertainty is on the group ranges we can approximate the uncertainty σ_B on \hat{B}_L from each sample i , by

$$\begin{aligned} \sigma_B^i &\approx \sqrt{\sigma_{\hat{P}_1}^2 + \sigma_{\hat{P}_2}^2 + \sigma_{\hat{L}_1}^2 + \sigma_{\hat{L}_2}^2 - 2 \text{cov}(\hat{L}_1, \hat{L}_2) - 2 \text{cov}(\hat{P}_1, \hat{P}_2) + 2 \text{cov}(\hat{L}_1, \hat{P}_1) - 2 \text{cov}(\hat{L}_1, \hat{P}_2)} \\ &\approx \sqrt{\sigma_{\epsilon_{gr1}}^2 + \sigma_{\epsilon_{gr2}}^2 - 2 \text{cov}(\epsilon_{gr1}, \epsilon_{gr2})}_i \end{aligned} \quad (1.1.9)$$

and then, assuming no correlation between samples:

$$\sigma_B = \sqrt{\sum_j \left| \frac{w_j \sigma_B^j}{w_i} \right|^2} \quad (1.1.10)$$

If all samples have equal weights, w_i , and equal standard deviations, σ_B^i , we then get

$$\sigma_B = \frac{\sigma_B^i}{\sqrt{n}} \quad (1.1.11)$$

n being the number of samples.

Once the phase ambiguity has been determined, the uncertainty on the ambiguity becomes a bias in subsequent measurements, so the resulting accuracy on the determined ambiguity becomes

$$\beta'_B = \beta_B \pm \sigma_B \quad (1.1.12)$$

The *measured* TEC can be found from the following equation, where B_1 and B_2 are the ambiguities associated with the two carrier phases. B_1 and B_2 are the only terms that have been added to the TEC equation discussed earlier.

$$TEC = \frac{f_1^2 f_2^2 ((\hat{L}_1 + B_1) - (\hat{L}_2 + B_2))}{C(f_1^2 - f_2^2)} \approx \frac{f_1^2 f_2^2 (\hat{L}_1 - \hat{L}_2 - \hat{B}_L)}{C(f_1^2 - f_2^2)} \quad (1.1.13)$$

The TEC measurement accuracy β_{TEC} can now be estimated. From (1.1.1) and (1.1.2) we have

$$\begin{aligned} (\hat{L}_1 - \hat{L}_2 - \hat{B}_L) &= (B_2 - B_1) - \hat{B}_L + \int_1 (1 - C \frac{N_e}{f_1^2}) ds - \int_2 (1 - C \frac{N_e}{f_2^2}) ds + (\Delta\beta_{L1} - \Delta\beta_{L2}) \\ &\quad - \int_1 (K \frac{N_e B_0 \cos(\theta)}{f_1^3}) ds + \int_2 (K \frac{N_e B_0 \cos(\theta)}{f_2^3}) ds + \varepsilon_1 - \varepsilon_2 \end{aligned} \quad (1.1.14)$$

$$= -\beta'_B + C \frac{(f_1^2 - f_2^2)}{f_1^2 f_2^2} \int_0 N_e ds + \beta_R + \beta_{B_0} + (\Delta\beta_{L1} - \Delta\beta_{L2}) + \varepsilon_1 - \varepsilon_2 \quad (1.1.15)$$

where

$$\begin{aligned}\beta_R &= (\int_1 ds - \int_2 ds) + \frac{C}{f_2^2} (\int_2 N_e ds - \int_0 N_e ds) - \frac{C}{f_1^2} (\int_1 N_e ds - \int_0 N_e ds) \\ \beta_{B_0} &= -\int_1 (K \frac{N_e B_0 \cos(\theta)}{f_3^3}) ds + \int_2 (K \frac{N_e B_0 \cos(\theta)}{f_2^3}) ds\end{aligned}\quad (1.1.16)$$

is the ray path splitting bias term and the second order ionosphere bias term. So the equation for the TEC measurement accuracy β_{TEC} becomes

$$\beta_{TEC} = \frac{f_1^2 f_2^2}{C(f_1^2 - f_2^2)} (\beta_R + \beta_{B_0} - \beta'_B + \Delta\beta_{L1} - \Delta\beta_{L2}) \quad (1.1.17)$$

and the corresponding TEC measurement uncertainty is

$$\sigma_{TEC} = \frac{f_1^2 f_2^2 \sqrt{(\sigma_{\hat{L}_1}^2 + \sigma_{\hat{L}_2}^2 - 2 \text{cov}(\hat{L}_1, \hat{L}_2))}}{C(f_1^2 - f_2^2)} = \frac{f_1^2 f_2^2 \sqrt{\sigma_{\varepsilon_1}^2 + \sigma_{\varepsilon_2}^2 - 2 \text{cov}(\varepsilon_1, \varepsilon_2)}}{C(f_1^2 - f_2^2)} \quad (1.1.18)$$

6.2.2 Error Budget based on derived equations and simulations

In the table below the uncertainty on the TEC is calculated from the equations derived above, for three different carrier phase uncertainties. We have assumed, as it can be seen from the table, that there is no correlation between the two carrier phases and code phases. The two L-band frequencies $f_1=1.57542$ GHz and $f_2=1.22760$ GHz have been used in the calculations.

GPSOS SDRs		TEC uncertainties(σ_{TEC})
Carrier Phase \hat{L}_1	Uncertainty $\sigma_{\hat{L}_1}$	
0.1 mm/ 0.3 mm/ 1.0 mm		0.0013 TEC Units/ 0.0040 TEC Units/ 0.014 TEC Units
Carrier Phase \hat{L}_2	Uncertainty $\sigma_{\hat{L}_2}$	
0.1 mm/ 0.3 mm/ 1.0 mm		
Carrier Phase Correlation $r_L = \text{corr}(\sigma_{\hat{L}_1}, \sigma_{\hat{L}_2})$	0.0	

		σ_B
Code Phase \hat{P}_1	0.1 m/ 0.3 m/ 1.0 m	
Uncertainty $\sigma_{\hat{P}_1}$		0.051 TEC Units/
Code Phase \hat{P}_2	0.1 m/ 0.3 m/ 1.0 m	0.153 TEC Units/
Uncertainty $\sigma_{\hat{P}_2}$		0.509 TEC Units
Code Phase Correlation $r_p = \text{corr}(\sigma_{\hat{P}_1}, \sigma_{\hat{P}_2})$	0.0	
Number of samples n	700	
Difference in clock errors for carrier phases \hat{L}_1, \hat{L}_2	$\Delta\beta_{L1} - \Delta\beta_{L2}$	0.0
Difference in clock errors for code phases \hat{P}_1, \hat{P}_2	$\Delta\beta_{P1} - \Delta\beta_{P2}$	0.0
Accuracy term	β_B^i	TBD
Accuracy term	β_B	TBD
Accuracy term	β_B'	TBD
Relative ray path splitting bias term	β_R / TEC	1.1 %
Relative second order ionosphere bias term	β_{B_0} / TEC	0.08 %
Relative accuracy on TEC meas- urement	β_{TEC} / TEC	1.2 %

It is necessary to make some simplifications and assumptions in order to calculate the accuracy on the TEC measurement. The two bias terms β_R and β_{B_0} can be expressed in the following way

$$\begin{aligned}\beta_R &= \int_1 (1 - \frac{C}{f_1^2} N_e) ds - \int_2 (1 - \frac{C}{f_2^2} N_e) ds - C \frac{f_1^2 - f_2^2}{f_1^2 f_2^2} \int_0 N_e ds \\ \beta_{B_0} &\approx -KB_p \int_0 N_e ds \left(\frac{1}{f_1^3} - \frac{1}{f_2^3} \right)\end{aligned}\quad (1.1.19)$$

Since the largest contribution to the line integrals in equation (1.1.6) is found when the ray is in the vicinity of its tangent point, we have approximated the term $B_\theta \cos(\theta)$ with B_θ , the along-ray component of the magnetic field at the tangent point. B_θ has been set to 30 μ T representing the worst case. This value is a representative equatorial value for the magnetic field at an altitude of 100 km. The first two integrals in the equation for β_R , the L_1 and L_2 carrier phases, neglecting higher order terms, has been calculated for a given occultation with the use of a simulation program called ROSAP, developed at DMI. The line integral of the electron density over the straight line between the LEO and GPS satellite can be approximated by the phase delay, calculated at a very high fre-

quency. This frequency was selected to be 100 times the L1 carrier frequency. The ray will at this high frequency very closely follow the straight line between the satellites. Fig. 6.2.2.1 to fig 6.2.2.4 shows the results of these simulations. The two bias terms β_R and β_{B_0} has been calculated as a function of altitude. The sum of β_R and β_{B_0} gives the worst case accuracy on the TEC measurement β_{TEC} , because we can assume that the difference between the clock biases for the two frequencies f_1 and f_2 cancel. Fig. 6.2.2.1 and 6.2.2.3 shows the double Chapman ionosphere model used in the simulations corresponding to the conditions at daytime and nighttime solar maximum. Fig. 6.2.2.2 and 6.2.2.4 shows the result of the simulations. It's seen from fig. 6.2.2.2 that the relative TEC accuracy is around 0.012 for conditions (worst case) corresponding to solar maximum at daytime. Accumulated numerically errors in the calculations, see fig. 6.2.2.4, are the reason for the noise seen in the curves especially at high altitudes.

6.2.3 Primary and secondary EDRs

The uncertainties on the primary and secondary EDRs presented in this section are based on estimates from the literature.

The uncertainties on the measured primary EDRs are summarized in the table below.

Primary EDRs	Accuracy	Uncertainty
Vertical Electron Density Profiles*	(TBD)	10^4 cm^{-3}
Height of F2-Layer Peak	(TBD)	20 km
Height of E-Layer Peak	(TBD)	10 km
Scintillations S ₄	(TBD)	0.1
Scintillations	(TBD)	0.1 radian

*The uncertainty on the electron density profile is based on preliminary results by Hajj and Romans (1997).

The uncertainties on the measured secondary EDRs are summarized in the tables below. The uncertainties are calculated as the square root of the sum of the squares of all the contributing errors. The uncertainties for most of the secondary EDRs are calculated for two different extreme conditions. The first number, representing worse case conditions, includes conditions representative of daytime solar maximum conditions, relatively low SNR and low latitude. The low latitude means that the contribution to the refractivity from the water vapor is at a maximum. The second number, best case conditions, represent conditions with a nighttime solar maximum, a relatively high SNR, and high latitude tropospheric conditions where the influence of water vapor is at a minimum. h represents the altitude in the tables. Most of table numbers are extracted from curves made by E.R. Kursinski (1997), see reference list. The plots themselves can be found in appendix A.

The five main error sources, with the summarized effect showed in the tables, are

Thermal noise caused by noise in the receiver front end. This error type will increase with altitude. It is the measurement method that becomes more sensitive to thermal errors at increasing altitude, because thermal errors become large compared to the small impact on the signal caused by the atmosphere.

Local multipath which occurs when multiple images of the signal arrive at the antenna after scattering off structures in the vicinity of the antenna.

The upper integration limit for the Abel and hydrostatic integral. At high altitudes when there are no more data available the density and bending angle structures must be estimated by models and assumptions.

Horizontal variation in the refractivity causes an error, because spherical symmetry is assumed in the retrieval process.

Residual ionosphere error. The presently used calibration scheme removes most of this ionospheric effect, and this error type is only significant during the daytime solar maximum.

Secondary EDR	Uncertainty, fractional error, worst conditions	Uncertainty, fractional error, best conditions
Vertical Refractivity Profiles	<0.4% for 5km < h < 30km	<0.4% for 5km < h < 40km

These numbers have been extracted from the paper Observing Earth's atmosphere with radio occultation measurements using the Global Positioning by E.R. Kursinski et al.

Secondary EDR	Temperature error, worst conditions	Temperature error, best conditions
Vertical Temperature Profiles	<1 K for 8km < h < 30km <0.5 K for 10km < h < 20km	<0.6 K for 8km < h < 30km <0.4 K for 10km < h < 20km

These numbers have been extracted from the paper Observing Earth's atmosphere with radio occultation measurements using the Global Positioning by E.R. Kursinski et al.

Secondary EDR	Temperature error	Error in vertical moisture profiles (Water Vapor)
1. In Troposphere	0.3/1.0/3.0 K	0.075/0.25/0.75 mb

We have extracted the numbers in this table from the paper GPS Sounding of the Atmosphere from Low Earth Orbit: Preliminary Results by R. Ware et al (1996).

Refractivity

The accuracy of the refractivity measurement is limited by the thermal noise error for altitudes higher than 30 km, while horizontal variation in the refractivity limits the accuracy of the measurements for altitudes less than 25 km. The error in the refractivity measurement is less than 0.4 % for altitudes between 5 and 30 km.

Temperature

The accuracy of the temperature measurement is limited by the thermal noise and the Abel transform boundary value problem for altitudes higher than 40 km. At equatorial latitudes the high concentration of the water vapor limits the temperature accuracy for altitudes less than 8 km, while the temperature at high latitudes can be found with an error less than 2.5K for altitudes near the earth surface. The temperature accuracy is limited by horizontal variation in the refractivity for altitudes between 9 and 17 km. For altitudes between 17 and 40 km the accuracy is limited by contributions from thermal noise, local multipath and residual ionosphere. The residual ionosphere error term gives a significant error in the worst case, but it has little impact in the best case.

Moisture profiles

The table above shows the relation between an error in temperature and the corresponding error in the vertical moisture profile, so an error of 1.0 K gives an error of approximate 0.25 mbar. The best humidity data will be obtained in the middle and lower troposphere at low latitudes where profiles are expected to have a relative accuracy of 20 % for altitudes of up to 6 and 7 km, given independent temperature accuracies of 1.5 K.

6.2.4 Results of preliminary simulations

Fig. 6.2.4.1 to 6.2.4.8 show the results of preliminary simulations performed with the EGOPS simulation program. The influents of two different error types on the retrieved temperature profiles have been investigated. All the simulations are dry air simulations using the modified MSIS90 atmosphere model. All the profiles show the difference between the retrieved temperature and the originally used MSIS90 temperature. The bending angle retrieval and Abel Transform described earlier has been used in these simulations. The error type, sampling rate and the corresponding figures are summarized in the table below. Five different runs have been made for each of the entries in the table.

Error type	Error size	Sampling rate	Figure
Gaussian noise on phase	1 mm	10 Hz	6.2.4.1
Gaussian noise on phase	2.3 mm	50 Hz	6.2.4.2
Clock error, White noise, 1 sec Allan dev.	10^{-12}	10 Hz	6.2.4.3
Clock error, Flicker noise, 1 sec Allan dev.	10^{-12}	10 Hz	6.2.4.4
Clock error, White noise, 1 sec Allan dev.	10^{-12}	50 Hz	6.2.4.5
Clock error, Flicker noise, 1 sec Allan dev.	10^{-12}	50 Hz	6.2.4.6
Clock error, White noise, 1 sec Allan dev.	10^{-13}	50 Hz	6.2.4.7
Clock error, Flicker noise, 1 sec Allan dev.	10^{-13}	50 Hz	6.2.4.8

The retrieved temperature is in general found with a relative high error in these preliminary simulations. It is however expected that a statistical optimization algorithm applied to the bending angle retrieval process, currently under development, will improve the retrieved temperature profile approximately by a factor of 10.

It is seen from the figures that the temperature error increases, as expected, with the sampling rate, hence the signal bandwidth. The temperature retrieval process is in general more sensitive to Flicker clock noise than white noise. The temperature error level is also reduced substantially, both for white and Flicker clock noise, if the one sec Allan deviation is reduced by a factor of 10, see figure 6.2.4.5 to 6.2.4.8.

6.2.5 Preliminary simulations of electron density profiles

From preliminary simulations using a double Chapman layer model of the ionosphere the error on electron density profiles have been estimated. The carrier phases L_1 and L_2 from the forward modeling using ROSAP were added with both 1 mm and 3 mm uncorrelated Gaussian noise and the output from the inversion algorithm was compared with the model input electron density. In figure 6.2.5.1 and 6.2.5.2 the difference between the electron density from inversion and the model electron density is shown as a function of height. The solid curve is the difference with noise added, where as the dashed curve is the difference without noise i.e. it represents the numerical error. With 1 mm Gaussian noise the difference follow the numerical error, when 3 mm noise is added this correlation is broken. In both cases the absolute error is less than 0.20×10^4 electrons pr. cm^3 . Figure 6.2.5.3 and 6.2.5.4 show the relative difference between the electron density from inversion and the model. In the model chosen the F2 peak is at 300 km and the E layer peak is around 110 km. The F2 and E peaks can be reproduced almost perfectly and the relative error on the magnitude of the peaks is less than a few percent.

6.3 Instrument Sensitivity Analysis

External Data Errors.

External data sources for most algorithms are clock correction data and POD data. Furthermore, in two specific cases in-situ N_e and troposphere temperature can be input to algorithms for ionosphere and troposphere EDRs.

The electron density profile algorithm may use in-situ N_e as input. However, it is not required as an input in order to meet the requirements and the current assumption is not to use this observation.

The secondary algorithm for the water vapor profile requires as a possibility troposphere temperature data as input. The accuracy that can be provided for the water vapor profiles is about 20% for low latitudes up to an altitude of 8 km, given independent temperature observations of an accuracy of about 1.5 Kelvin. At high latitudes, where the water vapor content is low the above mentioned accuracy is only fulfilled up to 5 km during summer and 3 km during the winter season.

Errors in clock correction data are analyzed as a system clock error together with the instrument errors in the previous section. It is therefore not considered further here.

Errors in the POD solution are in the [SRD] required to be below 0.5 m for the position and below 0.5 mm/sec for the velocity. According to [KUR] a position error of this magnitude has no significant influence on the retrieved atmospheric parameters and can therefore be neglected.

Velocity errors however are according to [KUR] not without significance. Especially for the component of the velocity error projected along the ray path, which contributes directly as an erroneous Doppler frequency. For a velocity error as small as 0.05 mm/s the rms value of the temperature error are expected to be 0.3 K. The error will however decrease rapidly at lower altitudes.

Since position errors primarily affect the calculated altitudes in the retrieved EDRs, the worst case component of the position error is the radial position error. For POD error analysis we therefore specify the radial position error for the LEO and for the GNSS satellite, which then is applied to all rays in the simulated occultation.

For the velocity error analysis the specified parameter is the along-ray component of velocity error, which then is applied to the LEO satellite. This is due to the well-known fact, that drag perturbations makes POD for the LEO satellite significantly more difficult than for the GNSS satellites.

7. References

1. Hajj, G. 1997, "First Ionospheric Electron Density Profiles Obtained with the Global Positioning System", *Radio Science*, May issue.
2. Kursinski, E.R. et al., 1997, [KUR] "Observing Earth's atmosphere with radio occultation measurements using the Global Positioning", *Journal of Geophysical Research*, pages 23,429-23,465
3. Ware, R., et al. 1996, "GPS Sounding of the Atmosphere from Low Earth Orbit: Preliminary Results", *Bulletin of the American Meteorological Society*, pages 19-39
4. Bevis, M., S. Businger, S. Chiswell T.A. Herring, R.A. Anthes, C. Rocken, R.H. Ware, 1994, "GPS Meteorology: Mapping Zenith Wet Delays onto Precipitable Water", *Journal of Applied Meteorology*, 33, pp. 379-386.
5. [SRD] Sensor Requirement Document.
6. Basu, S., et al. 1988, "Ionospheric constraints on VHF/UHF communications links during solar maximum and minimum periods", *Radio Science* 23, page 363-378.
7. Booker, H. G., 1979, "The role of gravity waves in the generation of spread-F and ionospheric scintillations", *J. Atmos. Terr. Phys.* Vol 41, page 501-515.
8. Kelly, M. C., 1989, "The Earth's Ionosphere, Plasma Physics and Electrodynamics", Academic Pres, INC.

8. Figure Captions

- Figure 3.1 Altitude distribution of electron density in the ionosphere. The upper panel gives the situation in the daytime hours. While the bottom panel reveal the distribution at night.
- Figure 3.2 Diurnal change of foF2 and foE in summer and winter at a high latitude site in Alaska in the northern hemisphere.
- Figure 3.3 The top panel gives the equatorial anomaly outlined by the NmF2 contours (in electrons/cm³). The lower panels show the latitudinal variation of the electron density across the equatorial anomaly at various altitudes. The lower left panel originates from topside ionograms above h_{max}. While the lower right panel gives the profiles below h_{max} observed from an ionosonde on ground.
- Figure 4.1 Global variations of amplitude fading in scintillations during solar maximum and minimum conditions (Basu et al., 1988).
- Figure 4.2 Spectra of ionosphere irregularities and their intensity as function of wave number over spatial scale sizes covering from the electron gyro-radius to the radius of the Earth (Booker, 1979).
- Figure 4.3 Rocket observations of the spectral horizontal variations in the electron density of the ionosphere (Kelly, 1989). The high frequency part of the power spectrum is cut off due to limitations in the instrumentation.
- Figure 4.4 TEC retrieval from a GPS rising occultation observed by the GPS/MET experiment (Time: 22.20-22.30 UT; Date: 20. Feb. 1997). The latitude and longitude of the profile centers at 50° N and 80° W, respectively.
- Figure 4.5 Bending angle retrieval as function of altitude for a GSP/MET occultation, which took place at 22.20-22.30 UT on 20th February 1997.
- Figure 4.6 Simulations of the relative electron density profile errors using L1 without clock errors (dotted line) and the L1-L2 difference algorithm for the phase delay (full line) in order to eliminate the clock errors in the simulation. The model of the

ionosphere consisted of Chapman layers for the E and F2 region.

Figure 4.7

Retrieved ionospheric electron density profile differences when Gaussian noise of 1.0 mm has been added to the phase measurements (full line). The dotted line gives the unperturbed retrieved profile.

Figure 4.8

Calculated electron density profile for a GPS/MET occultation on 20th February 1997. The observations are the same as used in Figure 4 for the TEC profile.

Figure 4.9

Temperature profile obtained from the GPS/MET occultation no. 256 on 4th February 1997. The upper panel shows the temperature profile based on the geometrical optics inversion (GO) using the Abel transform and the Fresnel inversion (FI). The lower left panel gives the comparison with the ECMWF analysis temperature fields. While the lower right panel show the temperature differences between the ECMWF data and the Abel transform inverted profile (GO) and the ECMWF data and the Fresnel transform inverted temperature profile.

Figure 4.10

Temperature profile estimates resulting from GPS/MET occultation no. 70, 4th February 1997. The contents of the panels are similar to the content of Figure 9.

Figure 5.1

Geometry of occultation.

Figure 6.2.2.1

Double Chapman ionosphere model corresponding to the conditions at daytime solar maximum.

Figure 6.2.2.2

Relative accuracy for the TEC measurement at daytime.

Figure 6.2.2.3

Double Chapman ionosphere model corresponding to the conditions at nighttime solar maximum.

Figure 6.2.2.4

Relative accuracy for the TEC measurement at nighttime.

Figure 6.2.4.1

Simulation of temperature profile, with Gaussian noise on the phase.

Figure 6.2.4.2

Simulation of temperature profile, with Gaussian noise on the phase.

Figure 6.2.4.3

Simulation of temperature profile, with white noise clock error.

- Figure 6.2.4.4 Simulation of temperature profile, with Flicker noise clock error.
- Figure 6.2.4.5 Simulation of temperature profile, with white noise clock error.
- Figure 6.2.4.6 Simulation of temperature profile, with Flicker noise clock error.
- Figure 6.2.4.7 Simulation of temperature profile, with white noise clock error.
- Figure 6.2.4.8 Simulation of temperature profile, with Flicker noise clock error.
- Figure 6.2.5.1 Simulation of electron density with 1 mm Gaussian noise.
- Figure 6.2.5.2 Simulation of electron density with 3 mm Gaussian noise.
- Figure 6.2.5.3 Electron density profile with 1 mm Gaussian noise compared relative to model.
- Figure 6.2.5.4 Electron density profile with 3 mm Gaussian noise compared relative to model.

9. Figures

Figure 3.1

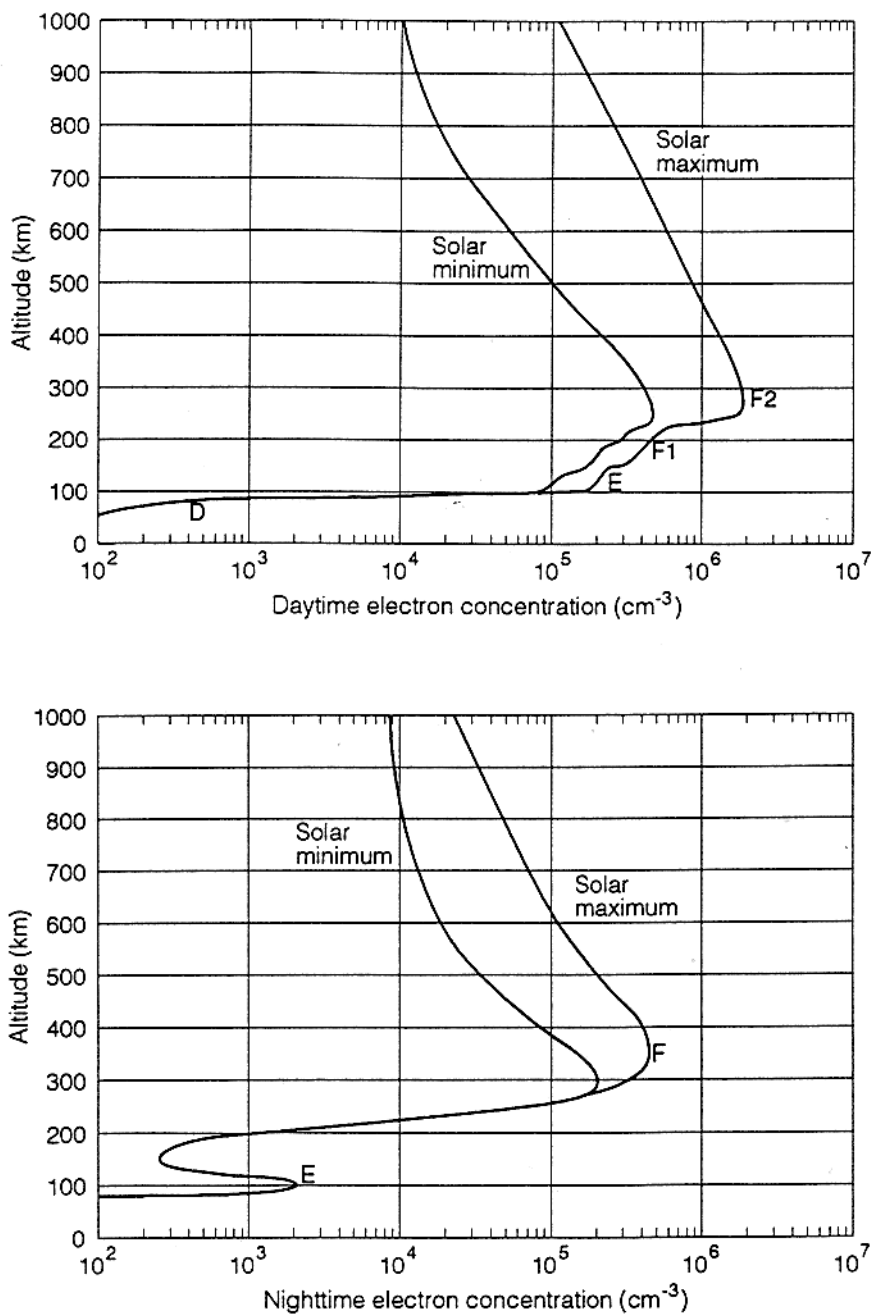


Figure 3.2

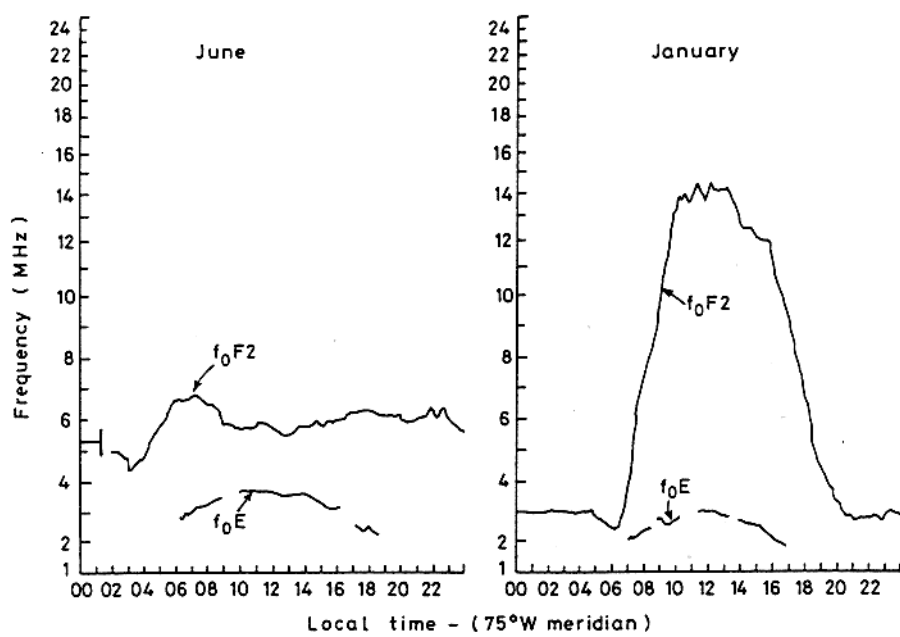


Figure 3.3

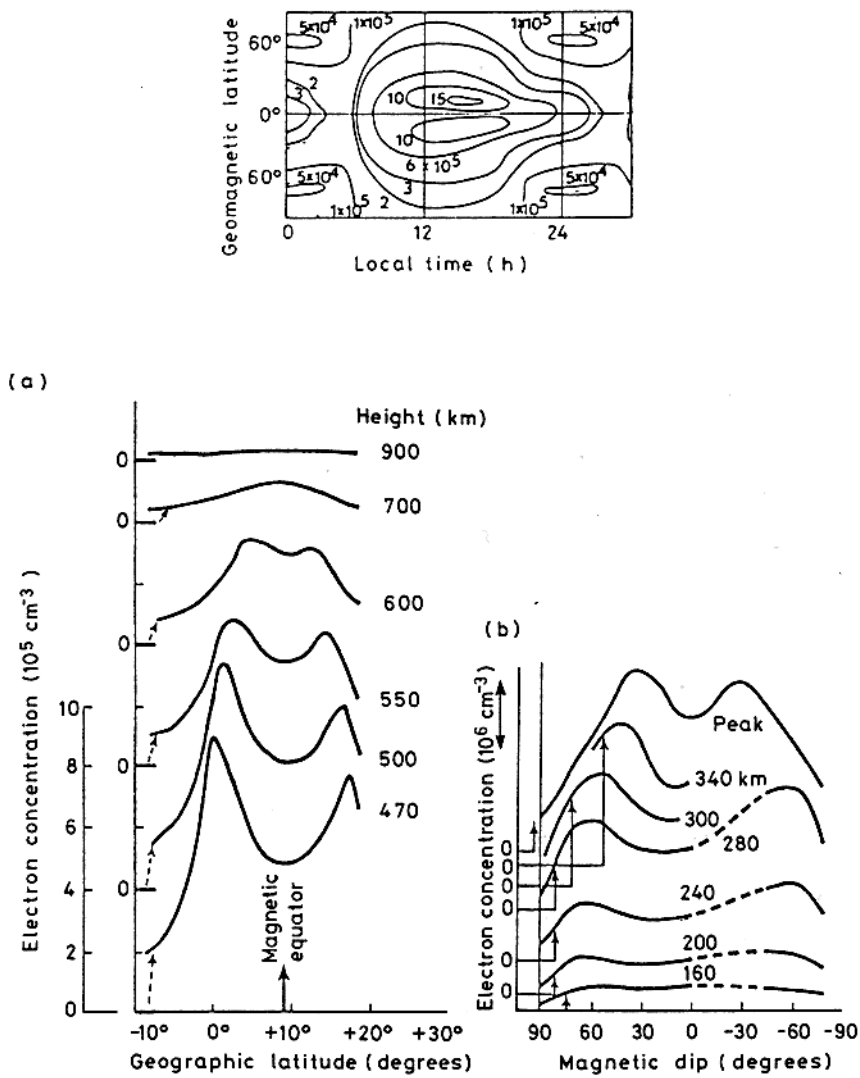


Figure 4.1

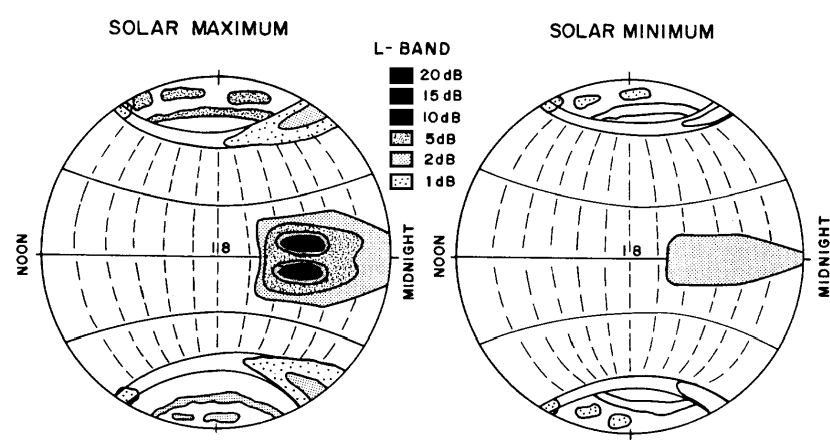


Figure 4.2

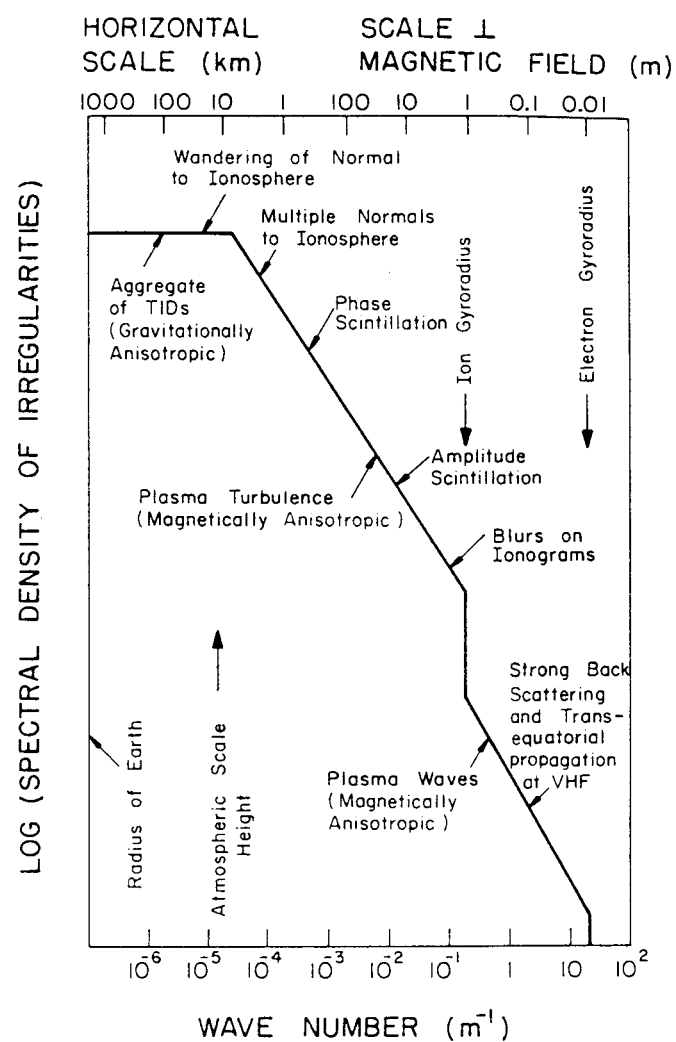


Figure 4.3

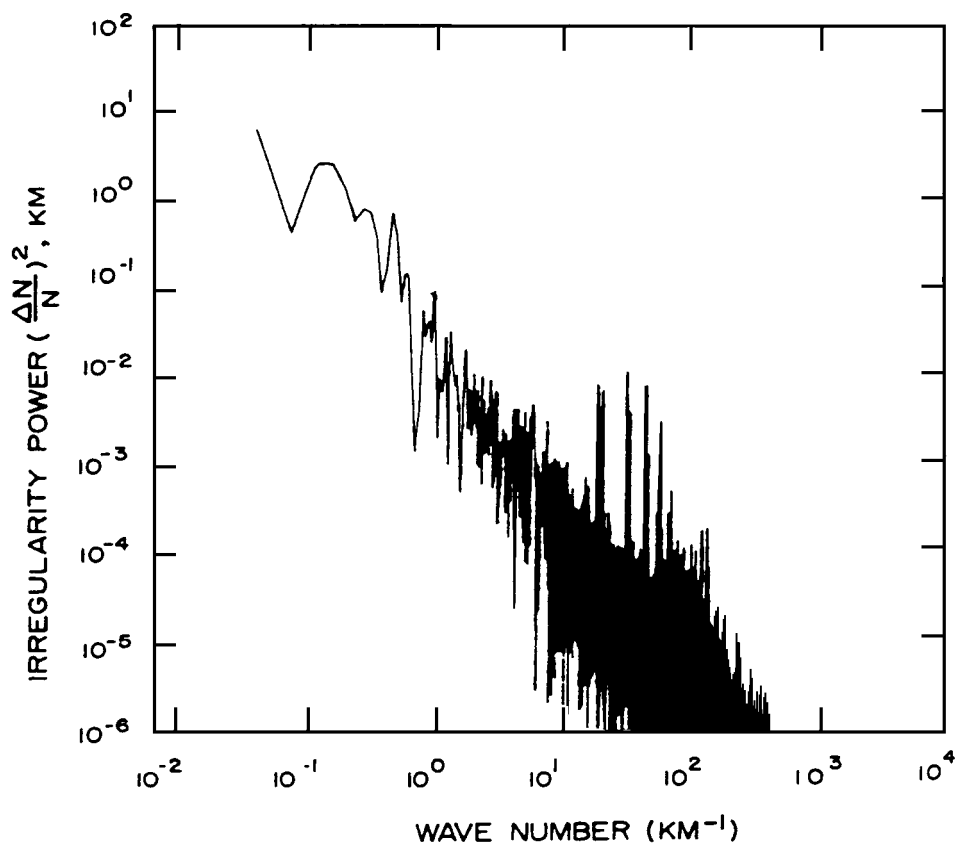


Figure 4.4

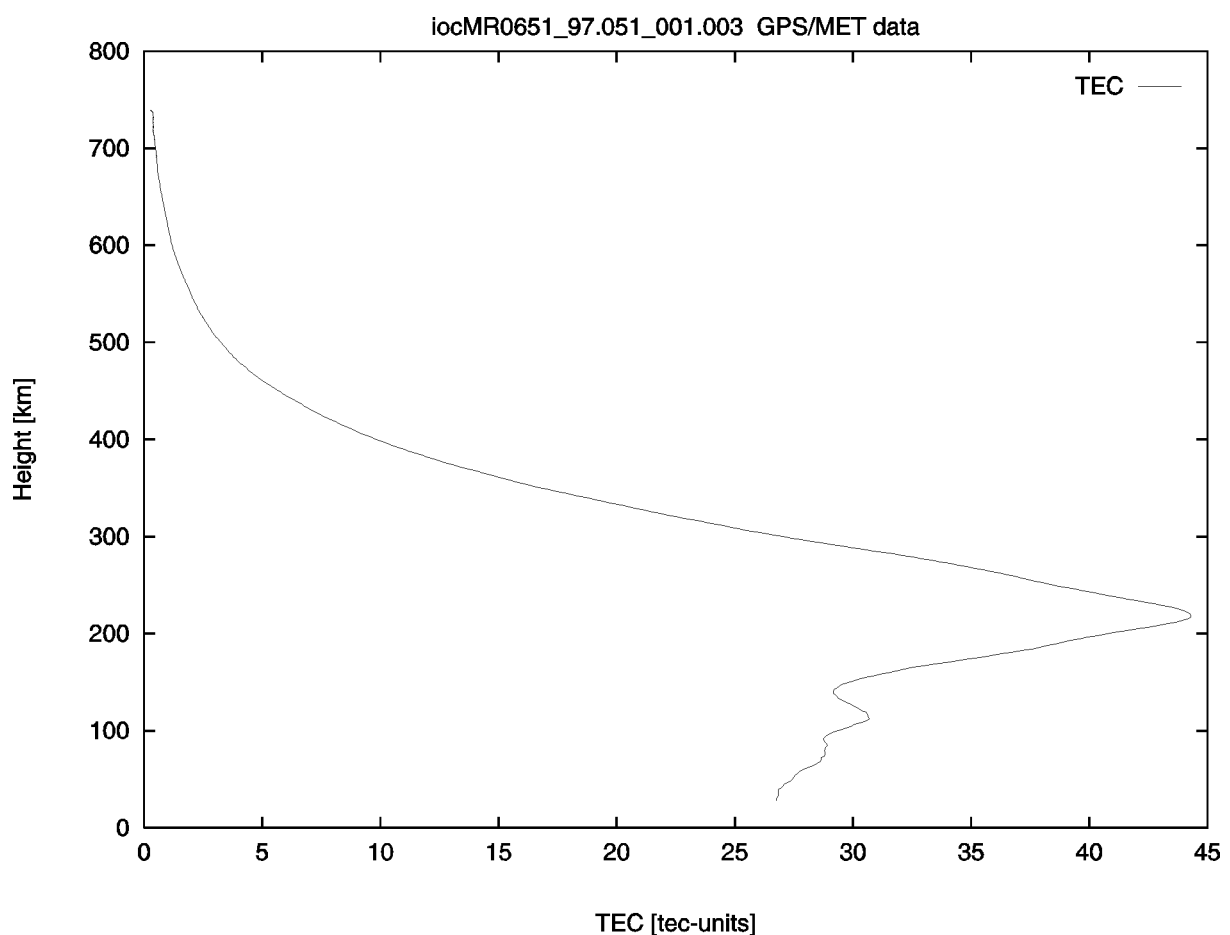


Figure 4.5

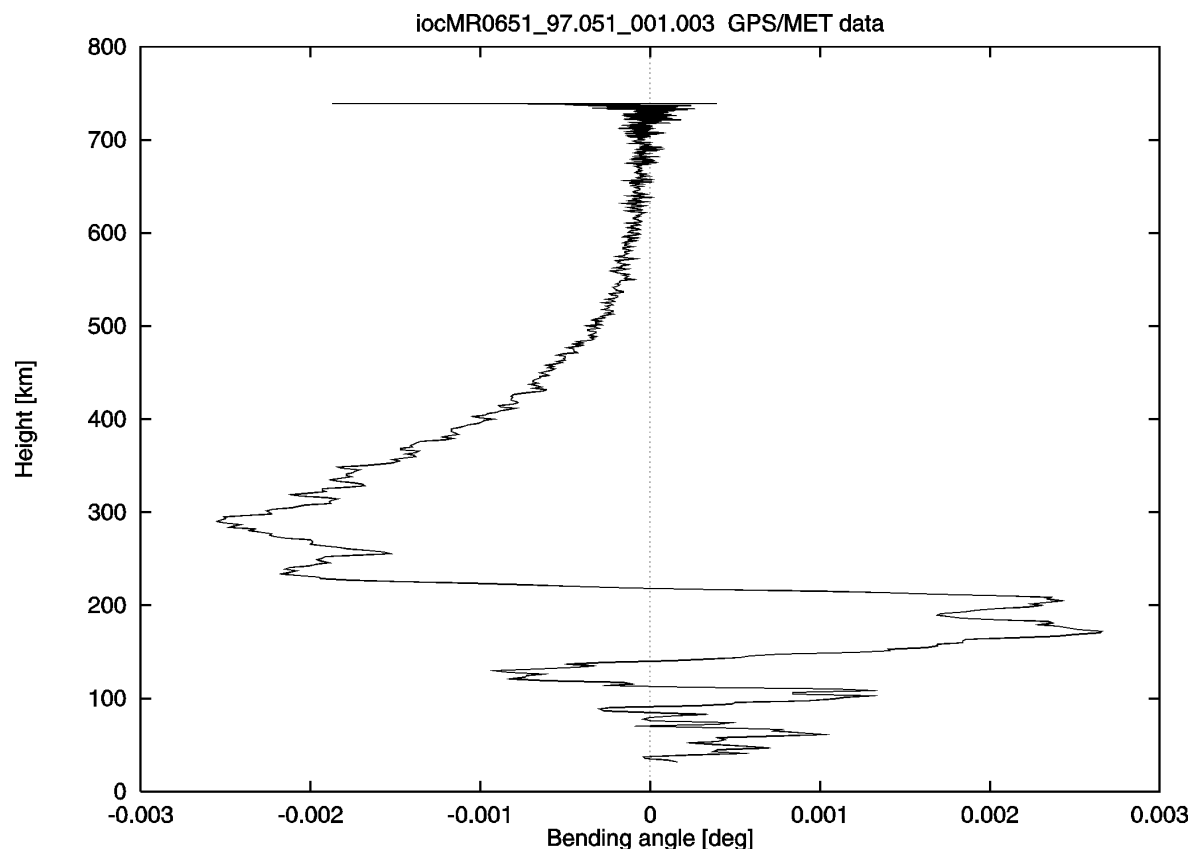


Figure 4.6

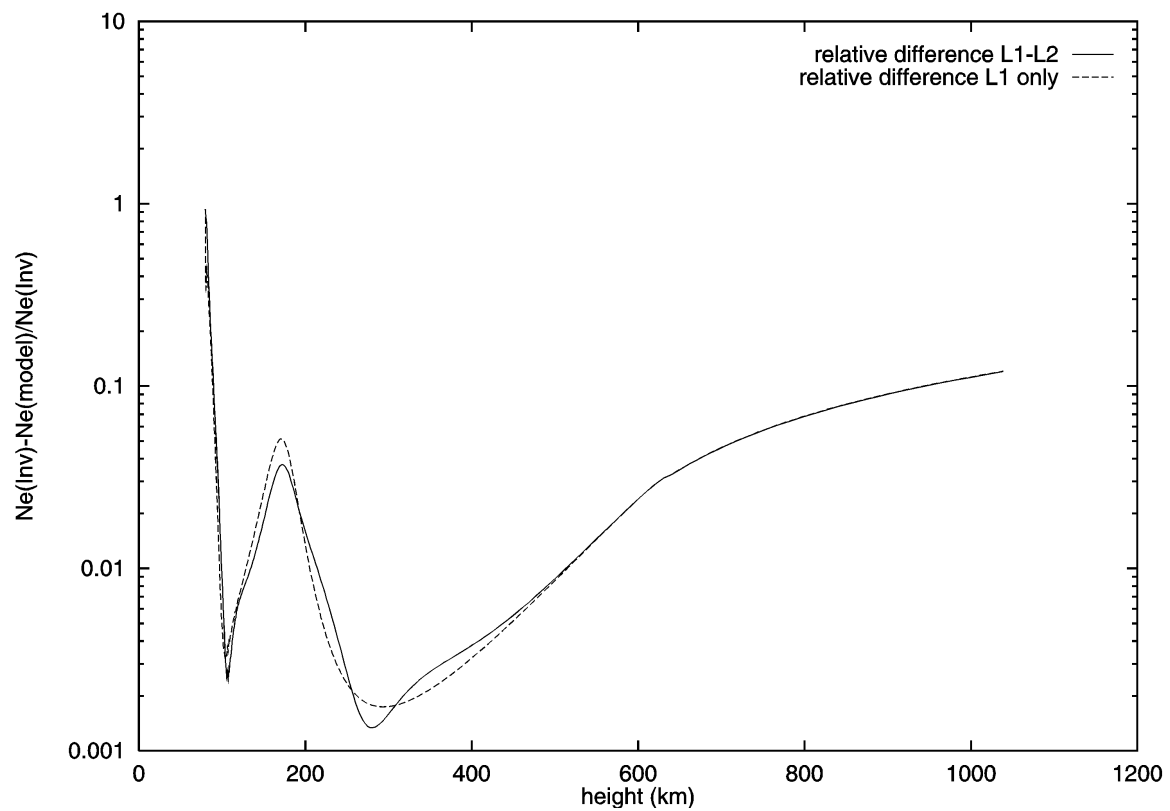


Figure 4.7

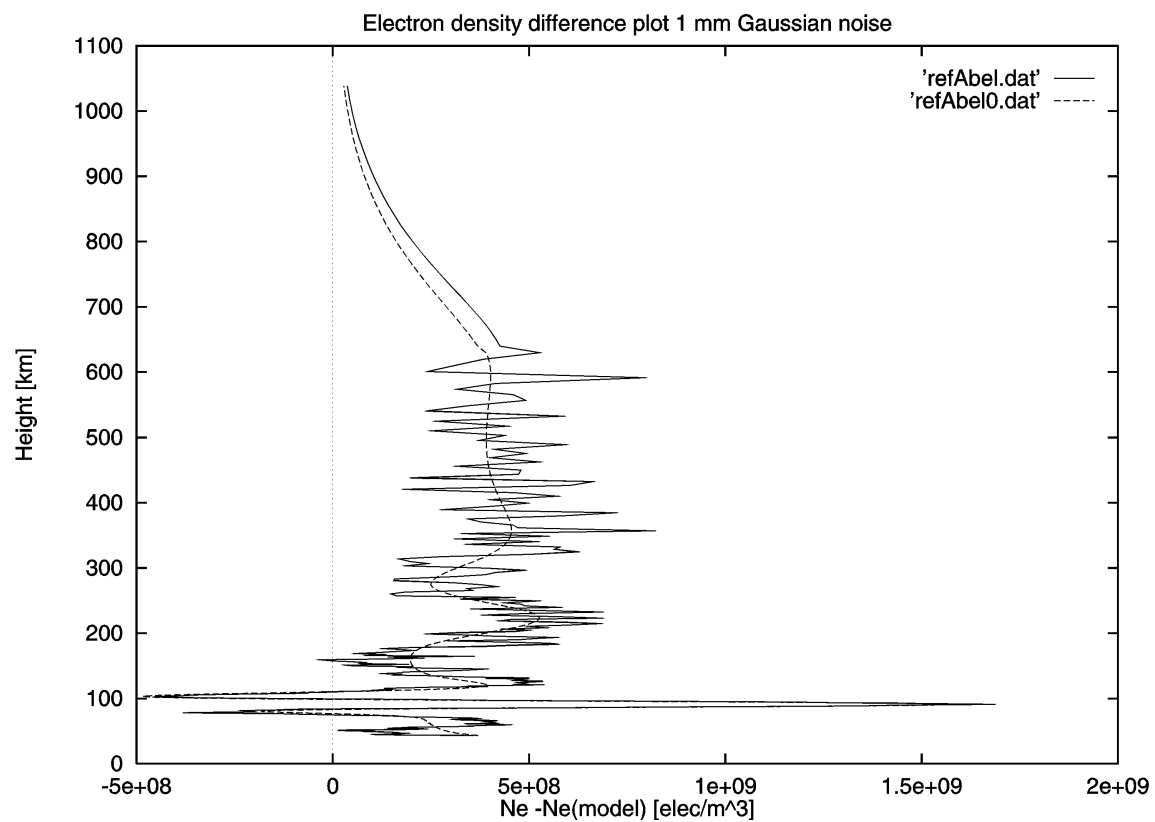


Figure 4.8

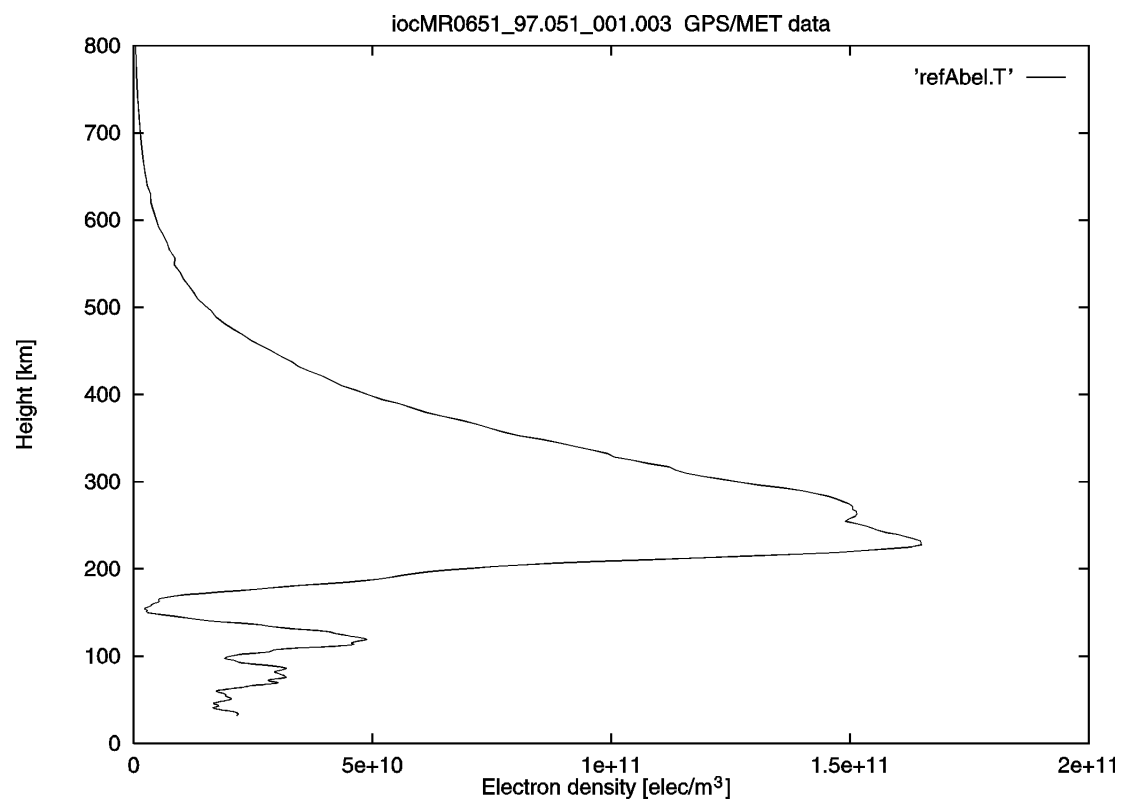


Figure 4.9

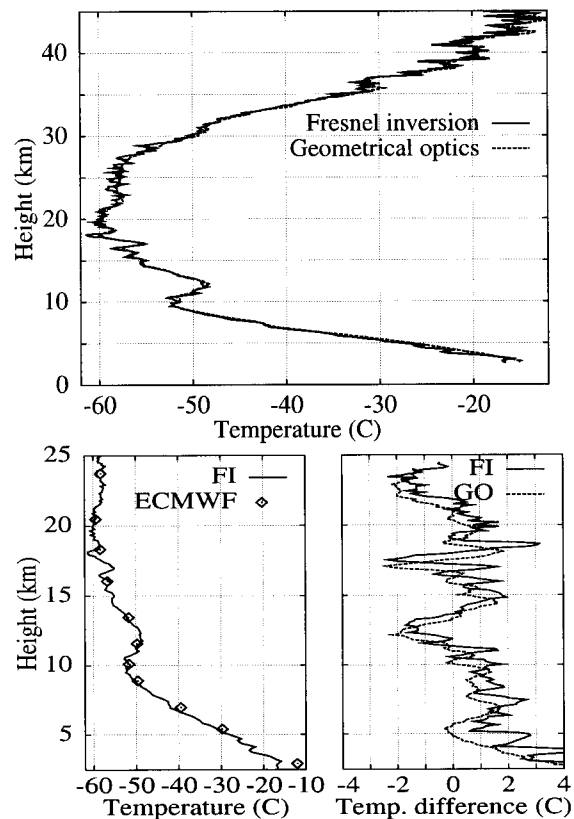


Figure 4.10

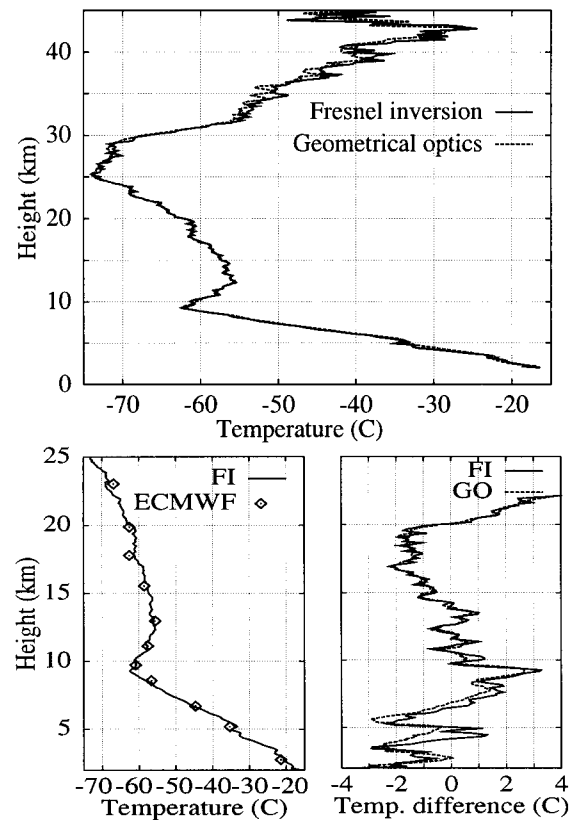


Figure 5.1

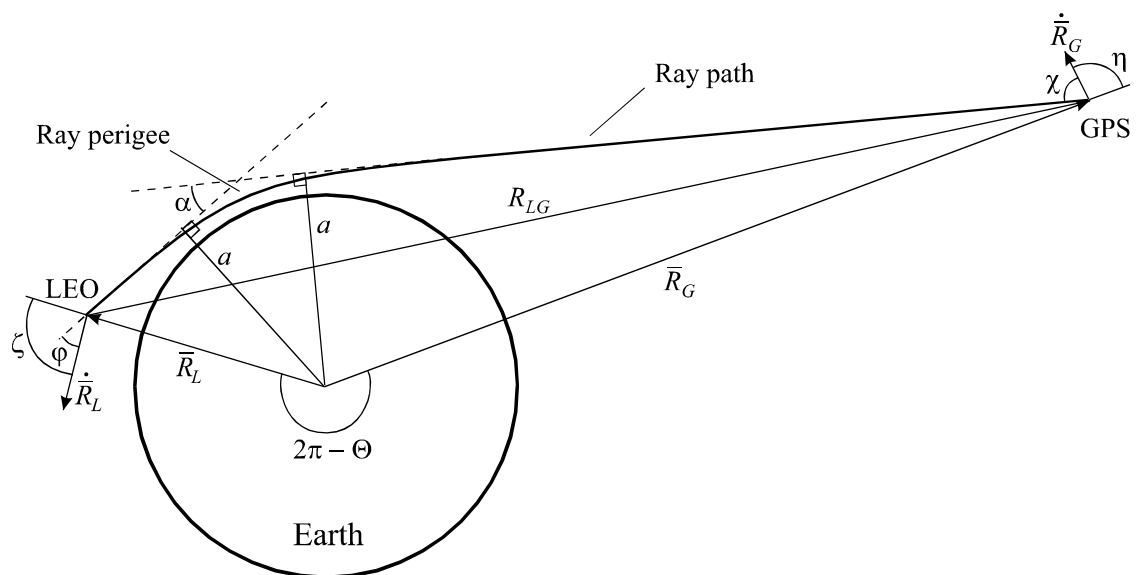


Figure 6.2.2.1

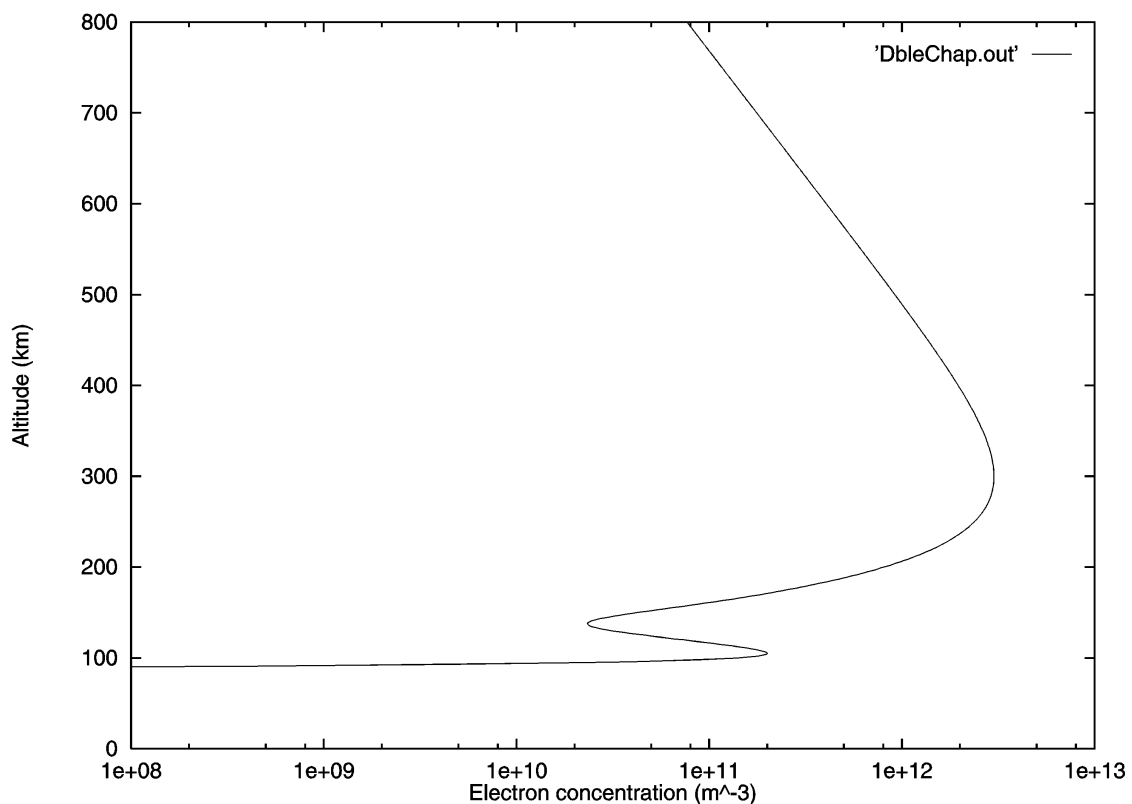


Figure 6.2.2.2

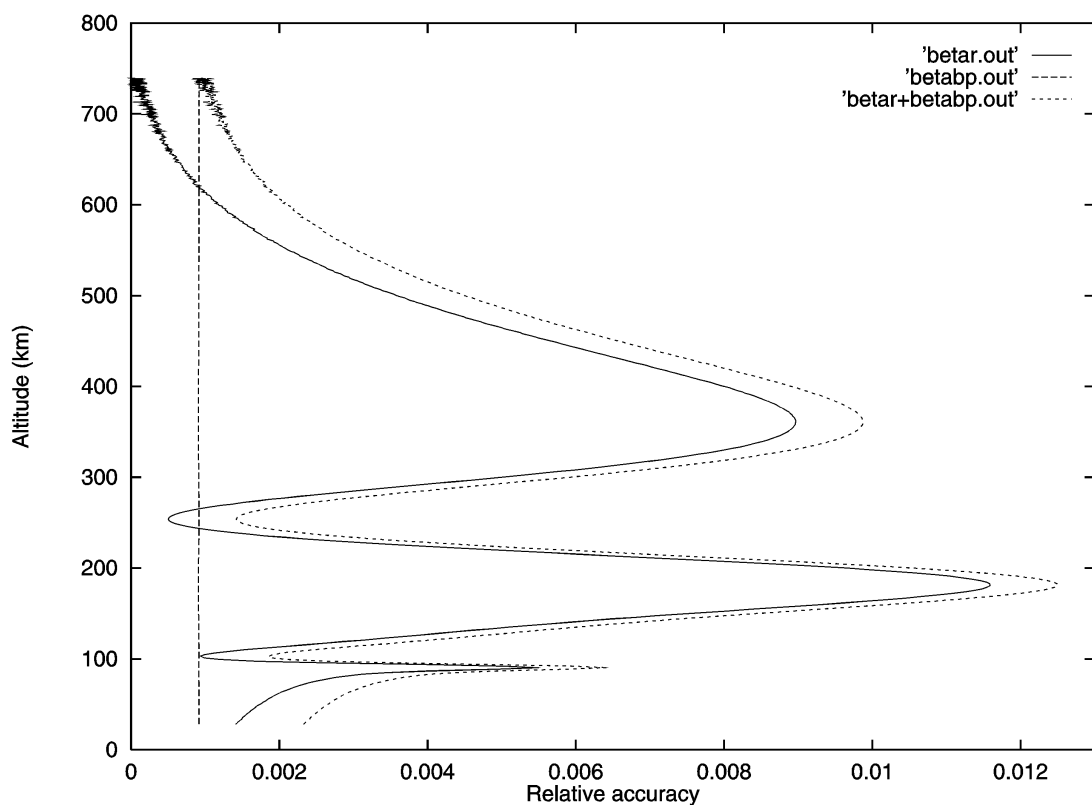


Figure 6.2.2.3

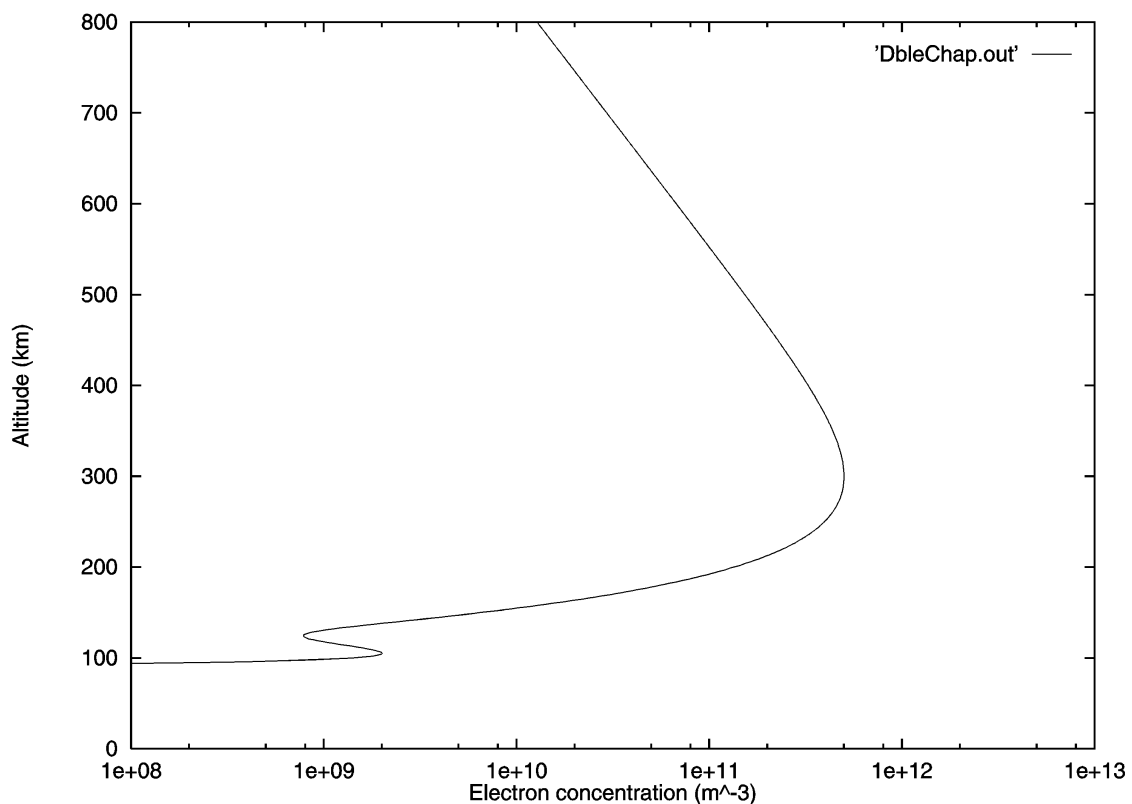


Figure 6.2.2.4

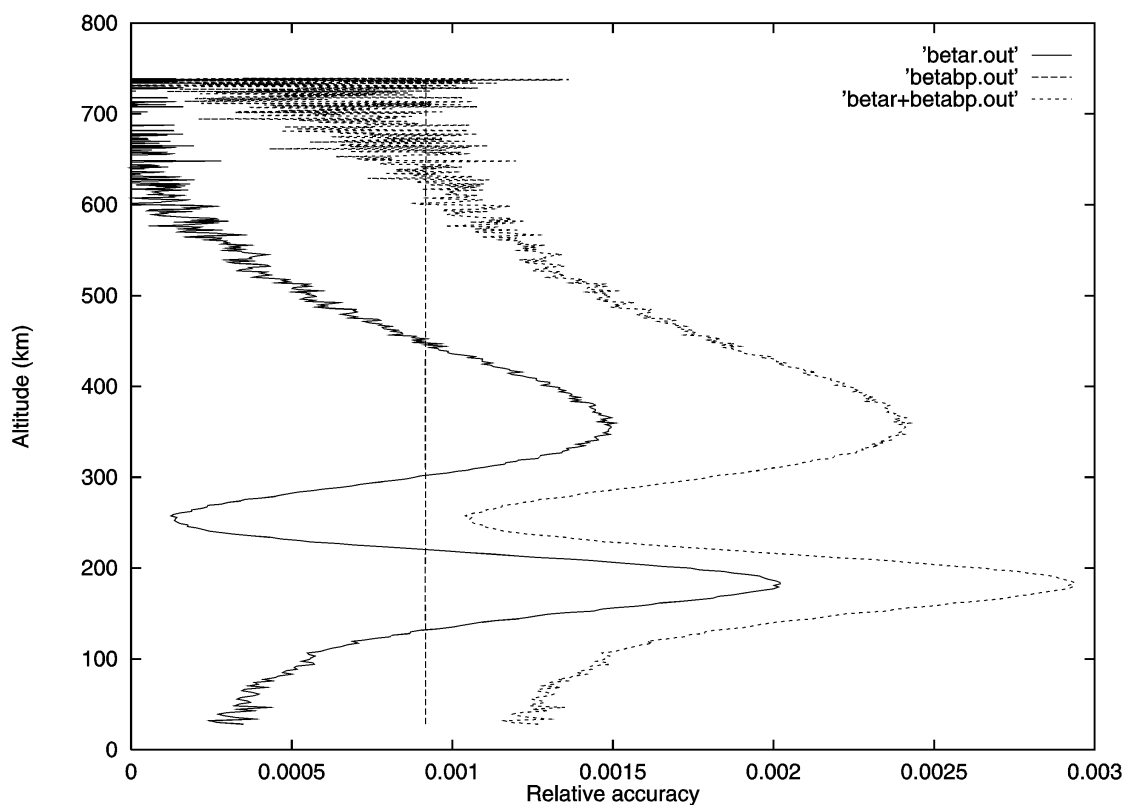


Figure 6.2.4.1

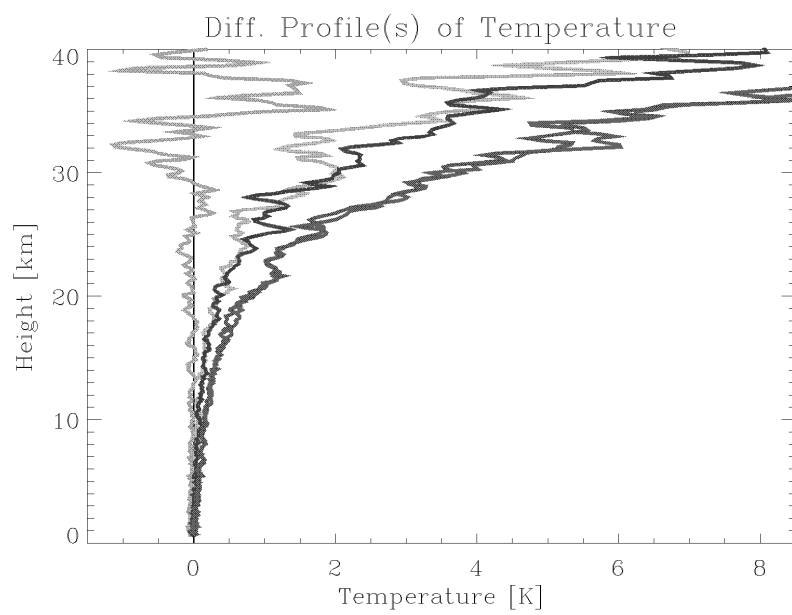
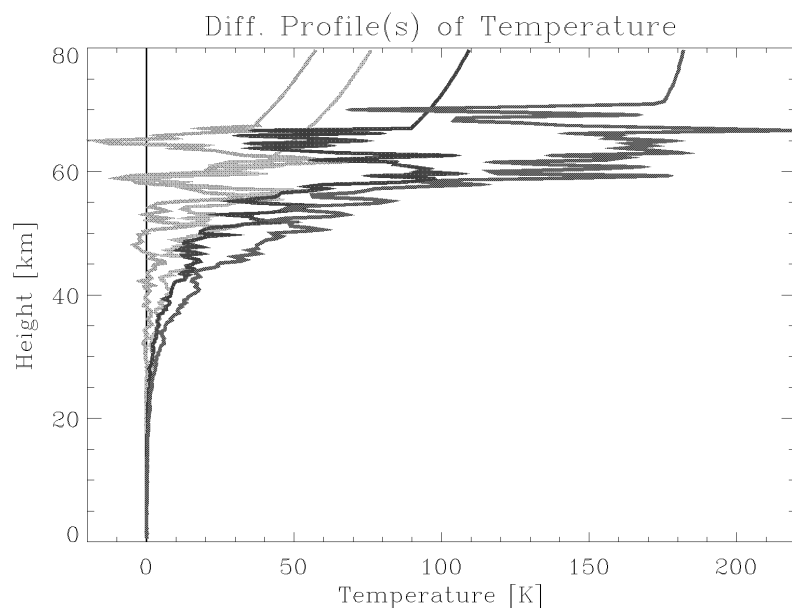


Figure 6.2.4.2

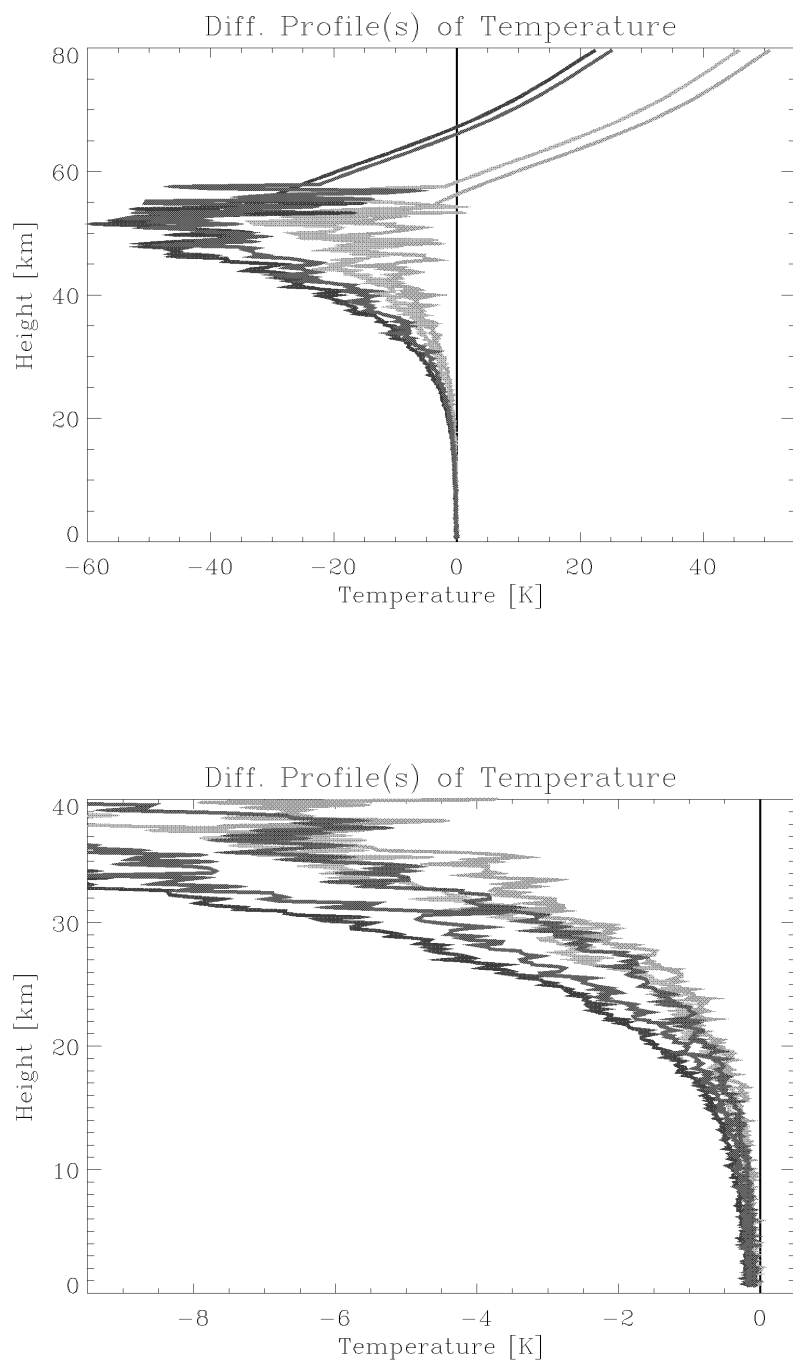


Figure 6.2.4.3

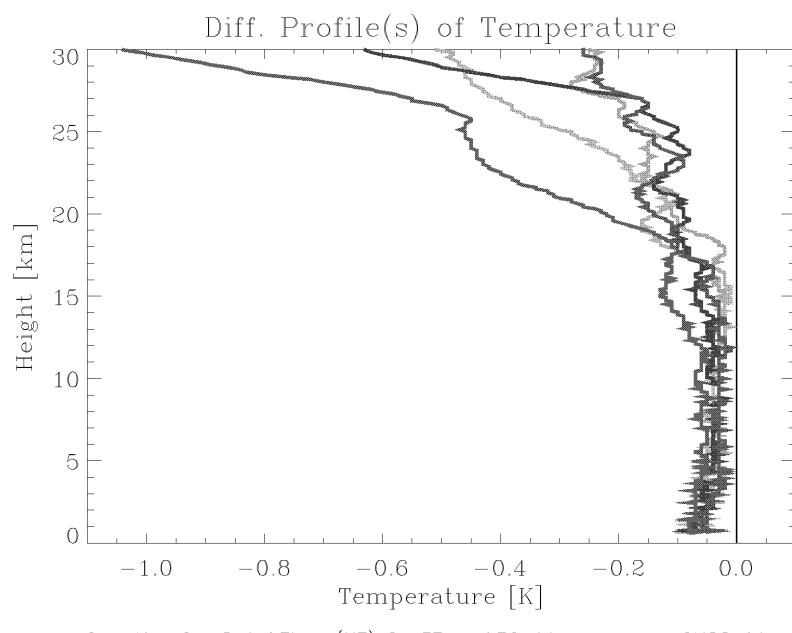
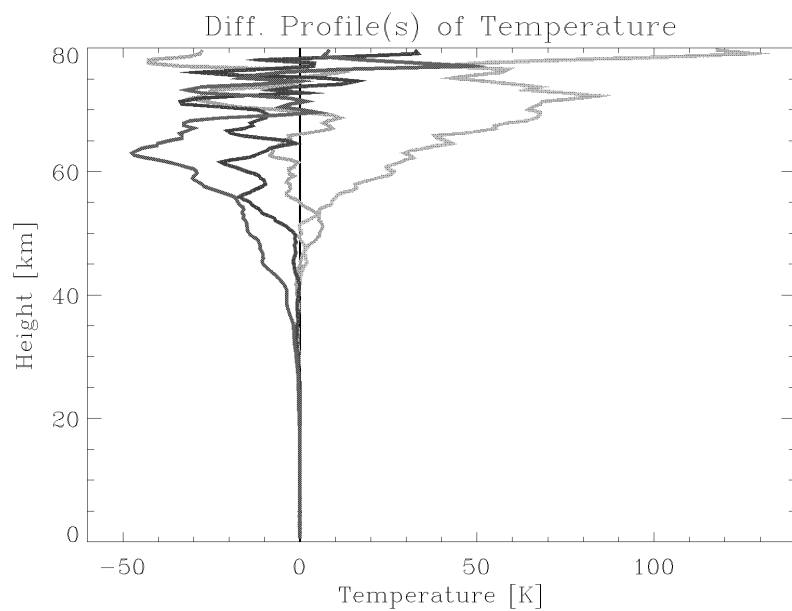


Figure 6.2.4.4

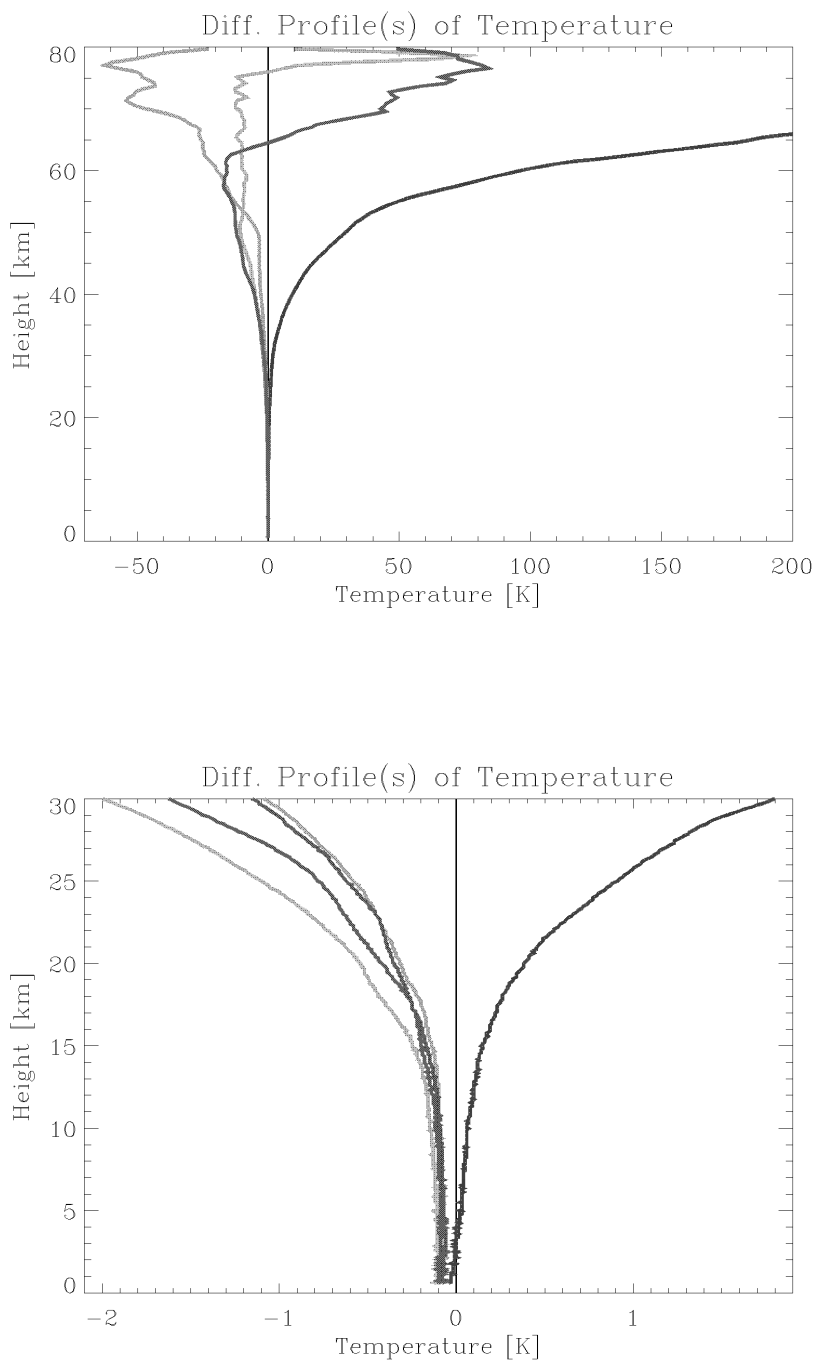


Figure 6.2.4.5

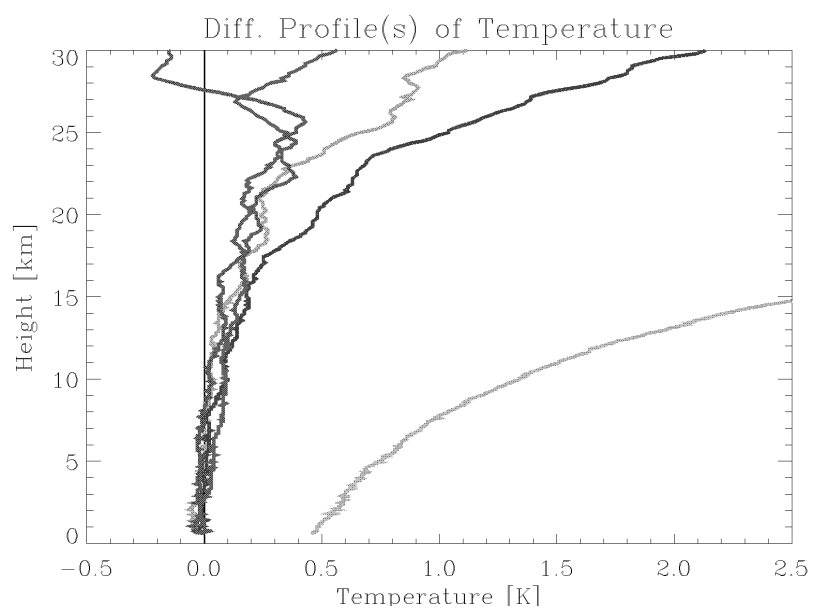
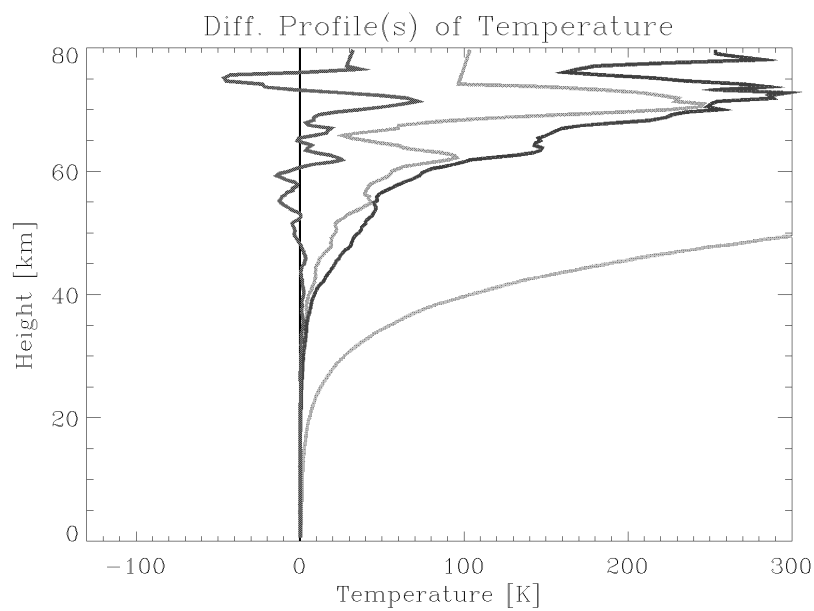


Figure 6.2.4.6

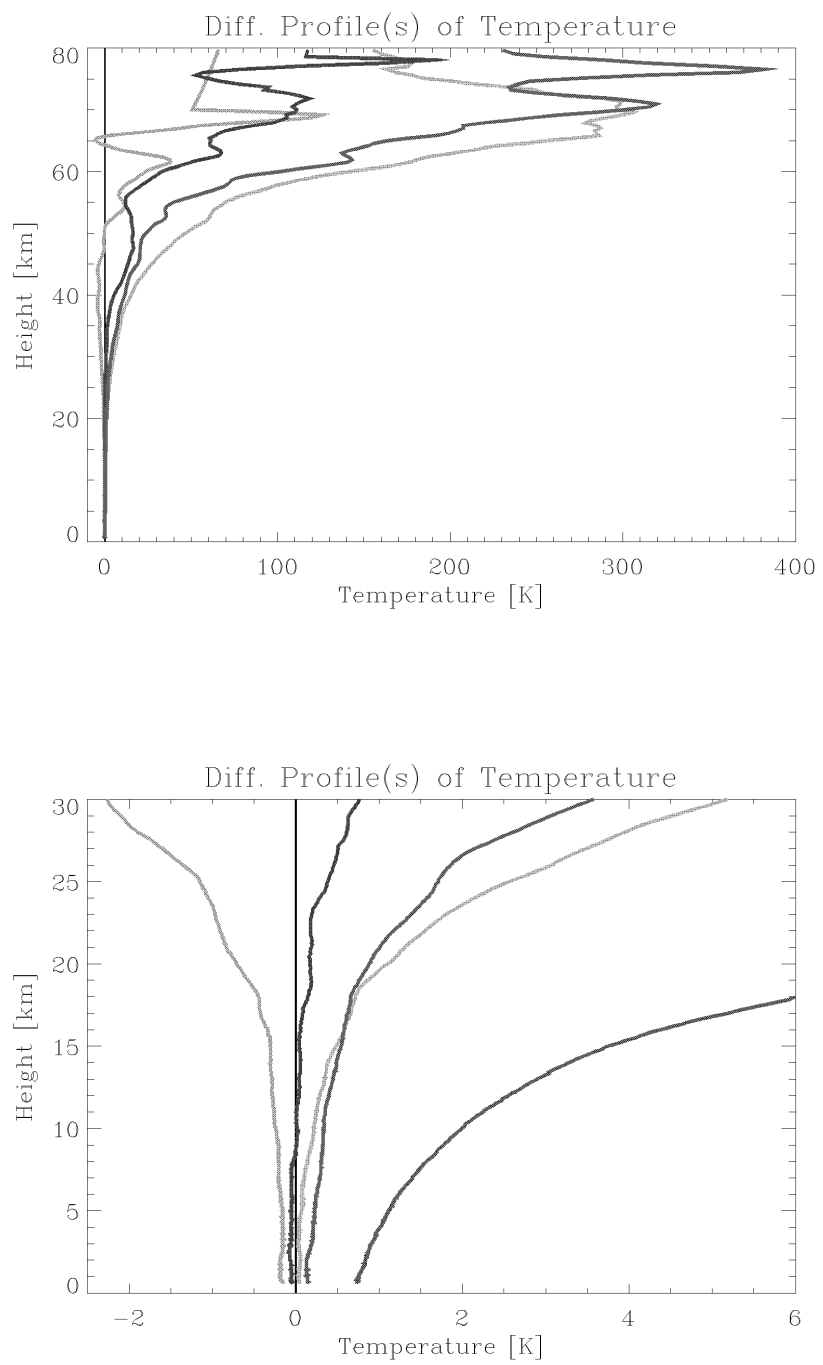


Figure 6.2.4.7

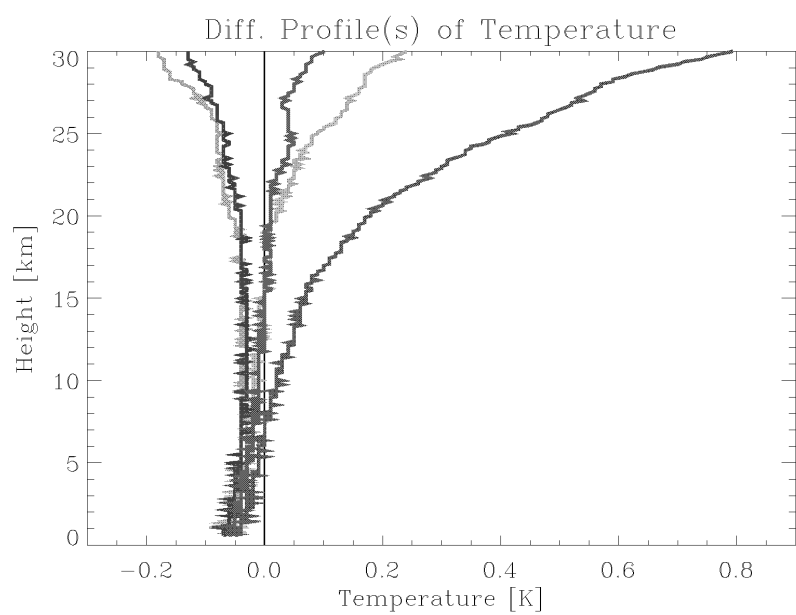
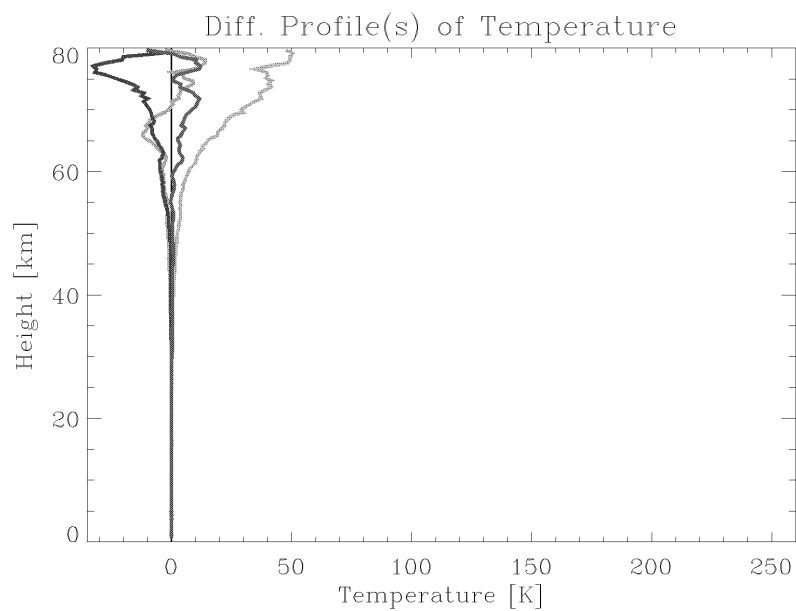


Figure 6.2.4.8

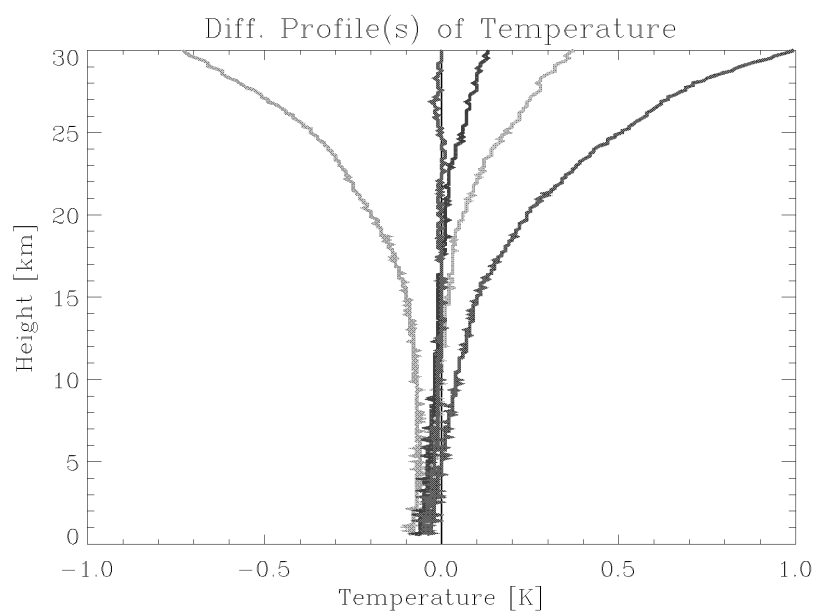
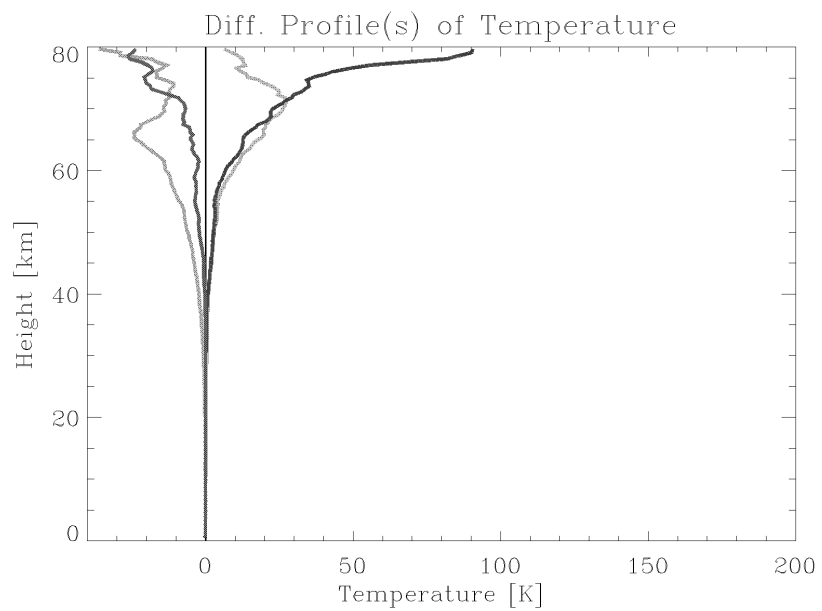


Figure 6.2.5.1

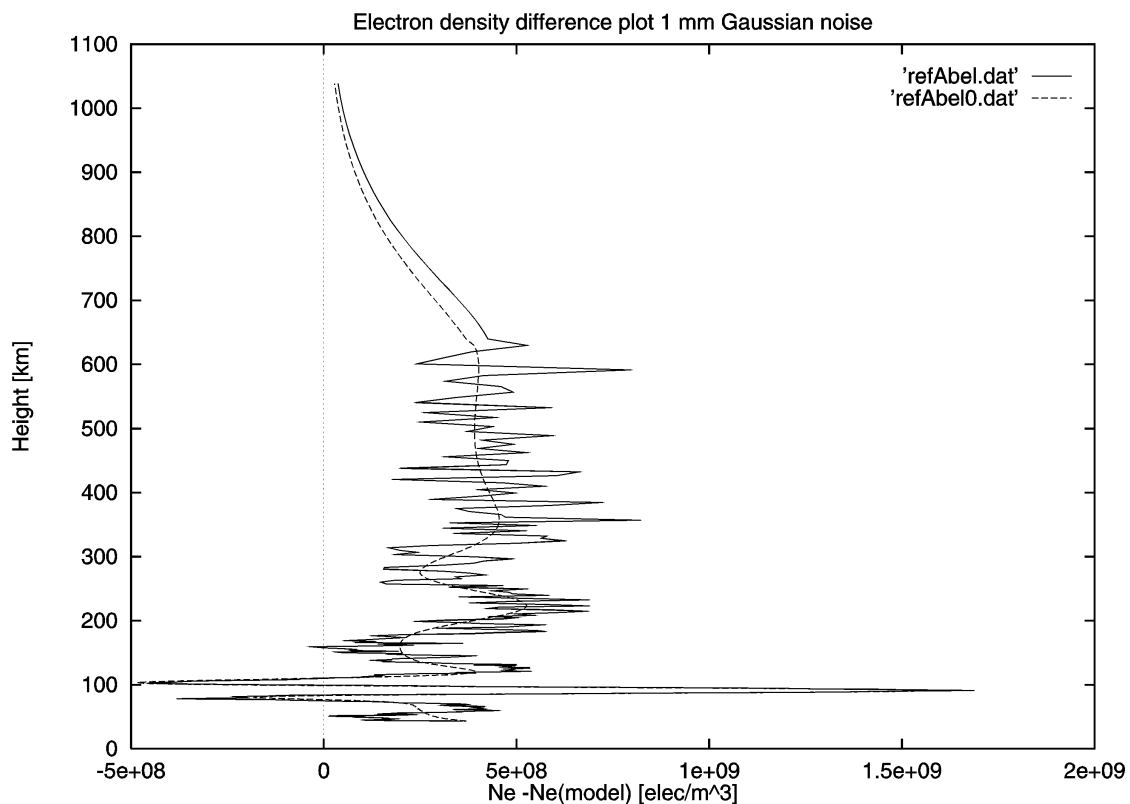


Figure 6.2.5.2

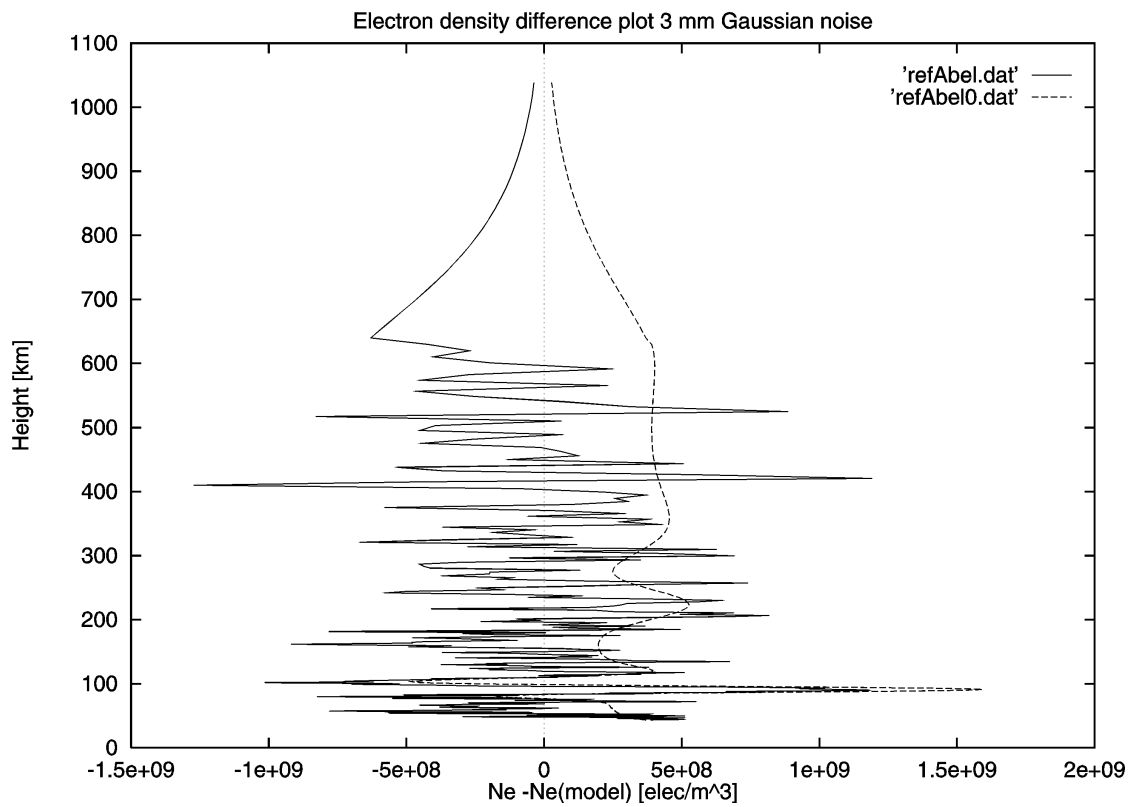


Figure 6.2.5.3

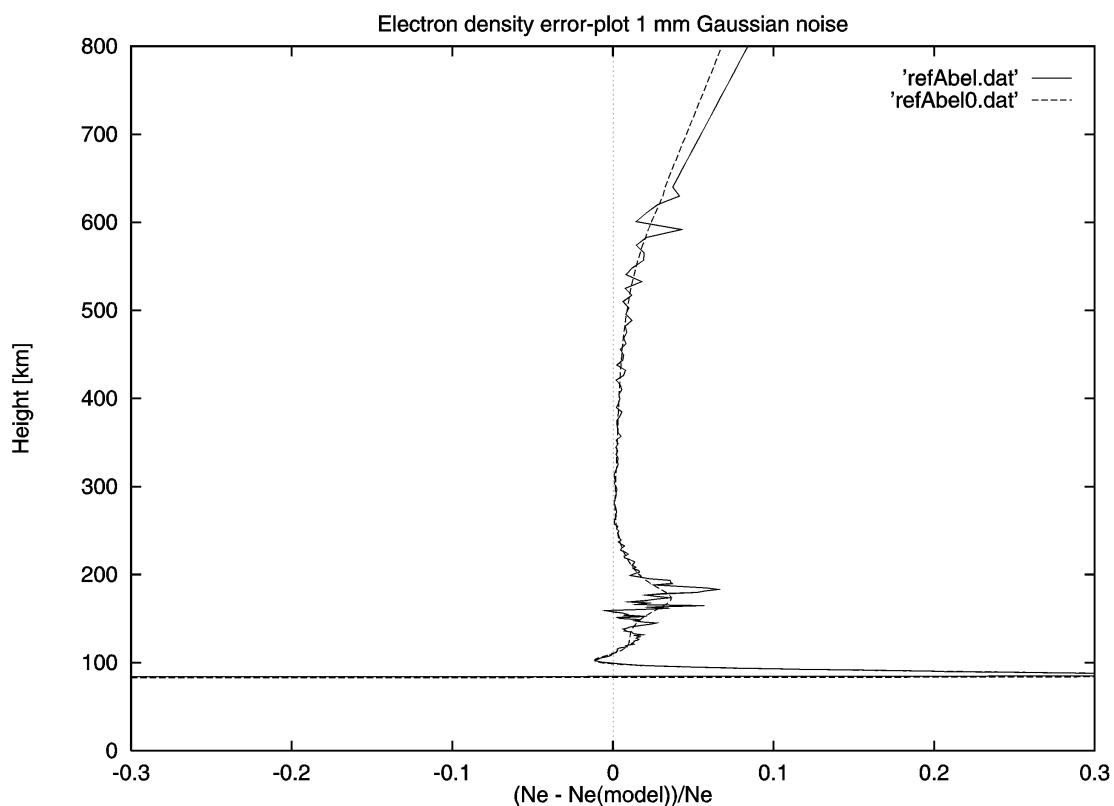
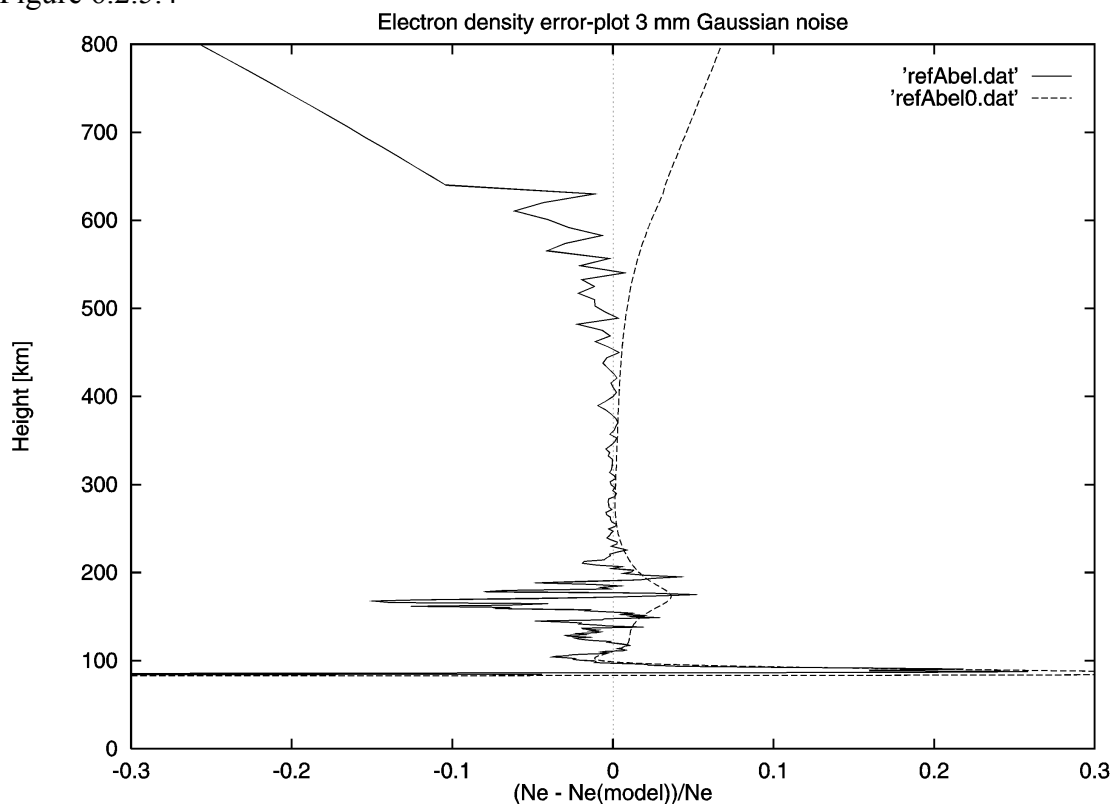


Figure 6.2.5.4



Appendix A

Figure 1A Refractivity error, worst case.

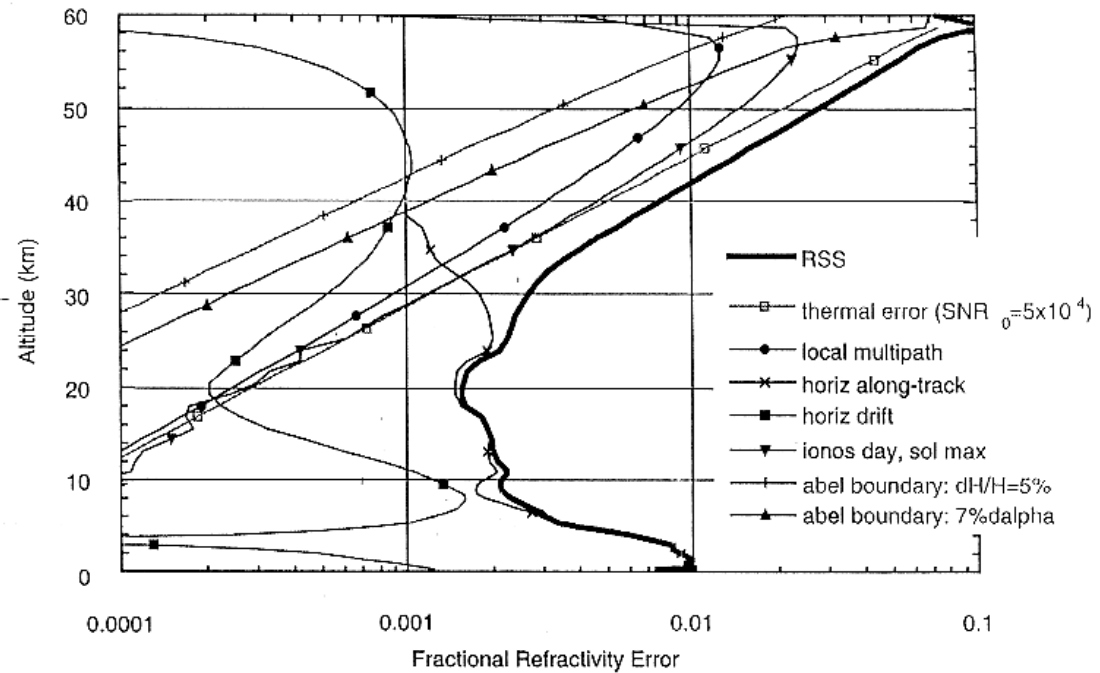


Figure 2A Refractivity error, best case.

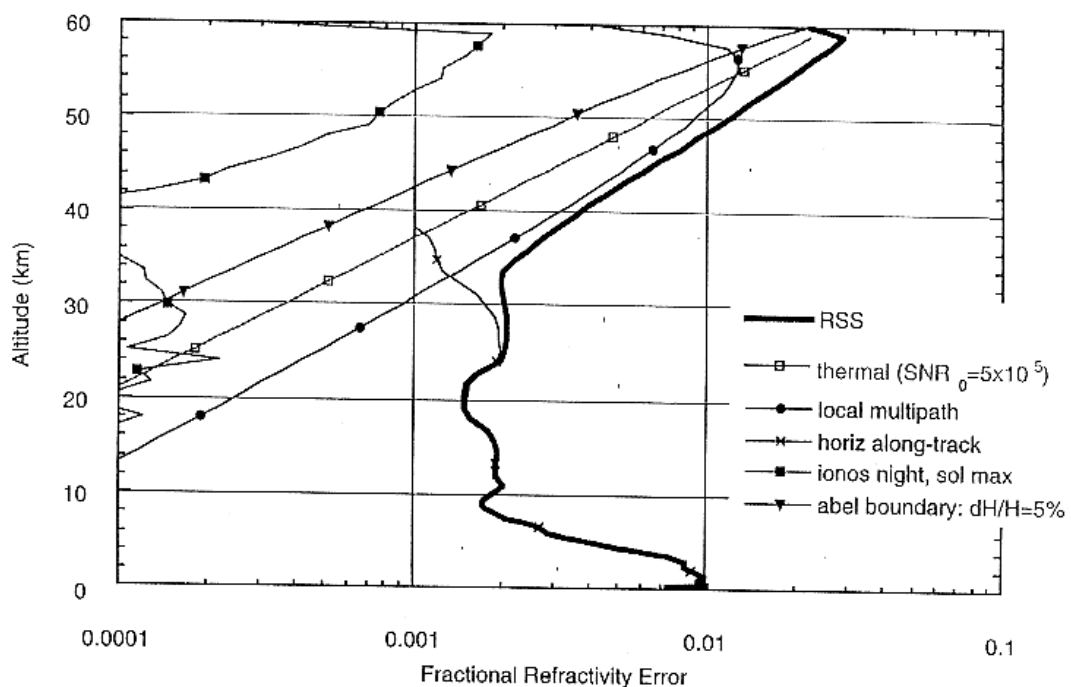


Figure 3A Temperature error, worst case.

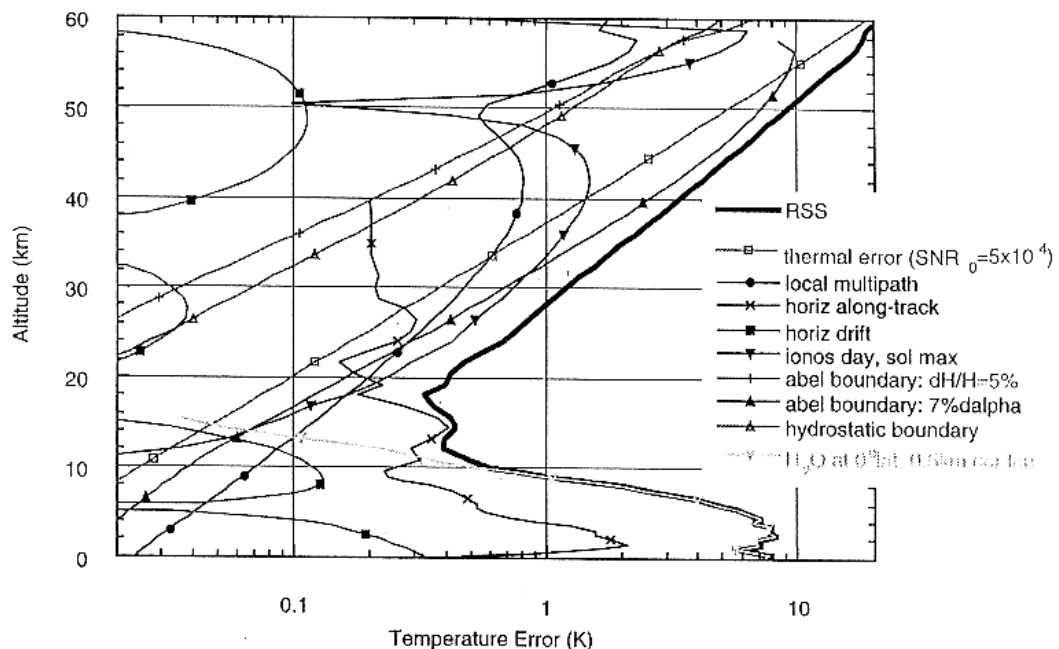
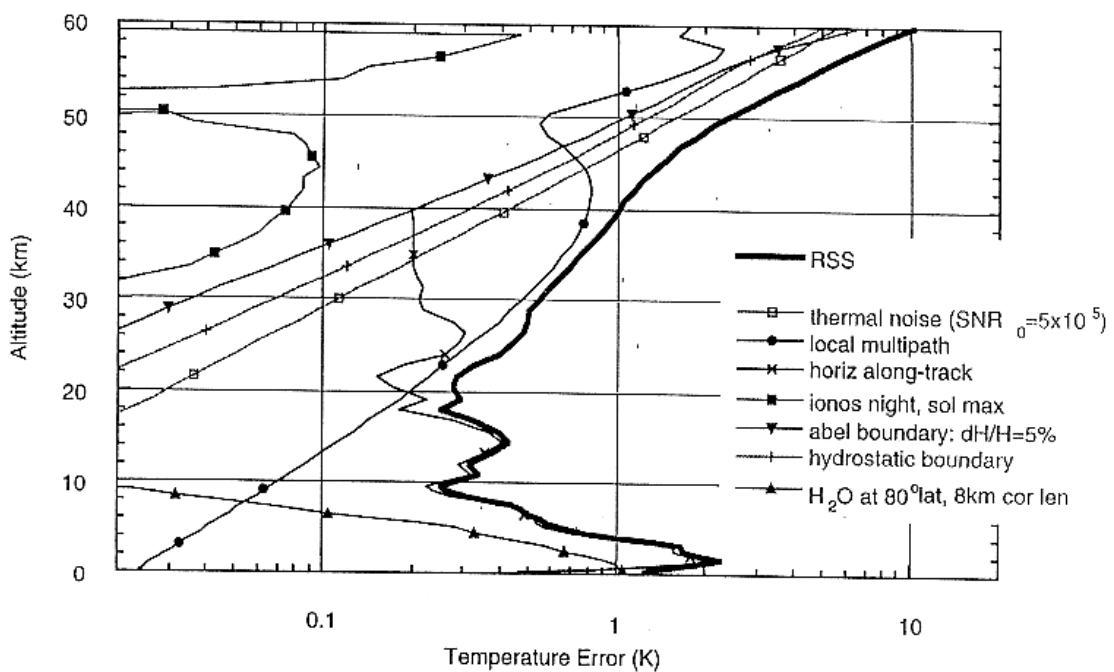


Figure 4A Temperature error, best case.



Appendix B

Electron Density Profiles/Ionospheric Specification

(I, -, ADTS)

Are HmE and HmF2 primary EDRs? If so, it should be mentioned specifically in the text.

Para. No.		Thresholds	Objectives
G40.8.5-1	a. Horizontal Reporting Interval (Not applicable to slant path TEC)	500 km	500 km
G40.8.5-2	b. Vertical Reporting Interval (Applicable to profile only)	10 km within 100 km of E/F peaks, 20 km elsewhere	3 km
	c. Horizontal Cell Size (Not applicable to slant path TEC)		
G40.8.5-3	1. 0-30/ latitude	400 km	100 km
G40.8.5-4	2. 30-50/ latitude	400 km	250 km
G40.8.5-5	3. 50-90/ latitude	400 km	50 km
G40.8.5-6	d. Vertical Cell Size (Applicable to profile only)	10 km within 100 km of E/F peaks, 20 km elsewhere	3 km
G40.8.5-7	e. Horizontal Coverage	Global	Global
G40.8.5-8	f. Vertical Coverage (Not applicable to slant path TEC)	90-600 km	60-800 km
	g. Measurement Range		
G40.8.5-9	1. Density profile	10^4 - 10^7 cm ⁻³	10^4 - 10^7 cm ⁻³
G40.8.5-10	2. Slant Path TEC	3-1000 TEC units	1-1000 TEC units
	h. Measurement Uncertainty		
G40.8.5-11	1. Density profile	10^4 cm ⁻³	10^3 cm ⁻³
G40.8.5-12	2. HmF2	20 km	5 km
G40.8.5-13	3. HmE	10 km	5 km
G40.8.5-14	4. Slant path TEC	3 TEC units	1 TEC unit
G40.8.5-15	i. Maximum Local Average Revisit Time (Not applicable to slant path TEC)	24 hrs	(TBD)

G40.8.5-1 The Horizontal Reporting Interval is here taken as the average of the horizontal spacing between profile locations for one satellite orbit. The threshold is to be confirmed (TBC) based on EGOPS simulations and 98% of all useful occultation events.

G40.8.5-3,4,5 Thresholds is based on the formula relating the horizontal and vertical resolution (e.g. Kurinski, 1997), the vertical resolution being determined by a 1 Hz sampling rate in the ionosphere.

G40.8.5-8,9,11 Thresholds based on preliminary results by Hajj and Romans (1997)

G40.8.5-12,13 Thresholds based on the vertical cell size and the fact that the E-layer peak is sharper than the F2-layer peak. (TBC) by simulations.

G40.8.5-15 Based on the horizontal cell size and the number of useful occultations (about 3200 per day) produced by 3 satellites.

Ionospheric Scintillation

(I, -, S)

Like TEC, Scintillations are an integrated effect over the path (NPOESS-GPS/GLONASS). Maybe TEC should be treated in this paragraph instead of in 3.2.1.1.3.1.2 above. We do not feel that the Horizontal Cell Size is applicable to scintillations nor TEC.

Para. No.		Threshold	Objectives
G40.8.11-1	a. Horizontal Cell Size	N/A	N/A
G40.8.11-2	b. Horizontal Coverage	Global	Global
	c. Measurement Range		
G40.8.11-3	1. S ₄	0.1-1.5	(TBD)
G40.8.11-4	2.	0.1-20 radians	(TBD)
	d. Measurement Uncertainty		
G40.8.11-5	1. S ₄	0.1	(TBD)
G40.8.11-6	2.	0.1 radian	(TBD)
G40.8.11-7	e. Local Time Range	20-24 hrs	(TBD)

G40.8.11-7 The threshold is based on observations by Basu *et al.* (1988).

Secondary GPSOS EDRs

(U, -, N)

We see secondary EDRs as EDRs that can be obtained from measurements by the GPSOS, and the EDRs have already been assigned as primary EDRs to another sensor.

It is unclear that the scientific algorithms for the secondary EDRs are TBS items.

It needs to be investigated if Precipitable Water should be a secondary EDR for the GPSOS. Vertical Atmospheric Refractivity Profiles should be added to the list of secondary EDRs.

Para. No.		Threshold	Objectives
G40.x.x-1	a. Horizontal Reporting Interval	500 km	500 km
	b. Vertical Reporting Interval		
G40.x.x-2	1. Troposphere	3-25 m	3-25 m
G40.x.x-3	2. Stratosphere	10-25 m	10-25 m
G40.x.x-4	c. Horizontal Cell Size	200 km	100 km
	d. Vertical Cell Size		
G40.x.x-5	1. Troposphere	0.2-1.0 km	3-25 m
G40.x.x-6	2. Stratosphere	1.0-1.5 km	10-25 m
G40.x.x-7	e. Horizontal Coverage	Global	Global
G40.x.x-8	f. Vertical Coverage	0-30 km	0-50 km
	g. Measurement Range		
G40.x.x-9	1. Refractivity profile	4-300 N unit	0.2-300 N unit
G40.x.x-10	2. Pressure profile	10-1100 mb	0.5-1100 mb
G40.x.x-11	3. Temperature profile	180-335 K	180-335 K
G40.x.x-12	4. Moisture profile	(TBD)	(TBD)
	h. Measurement Uncertainty		
G40.x.x-13	1. Refractivity profile	0.3 %	0.05 %
G40.x.x-14	2. Pressure profile	0.3 %	0.05 %
G40.x.x-15	3. Temperature profile	1 K	0.2 K
G40.x.x-16	4. Moisture profile	20 %	5 %
G40.x.x-17	i. Maximum Local Average Revisit Time	4 days	(TBD)

G40.x.x-1 The Horizontal Reporting Interval is here taken as the average of the horizontal spacing between profile locations for one satellite orbit. The threshold is to be confirmed (TBC) based on EGOPS simulations and 98% of all useful occultation events.

G40.x.x-2,3 Based on a 100 Hz sampling rate in the neutral atmosphere, and simulation studies in a multipath region.

G40.x.x-4,5,6 Thresholds is based on the formula relating the horizontal and vertical resolution (e.g. Kurinski 1997), the vertical resolution being determined by the first Fresnel diameter.

G40.x.x-4 Objective is based on the horizontal drift of the tangent point.

G40.x.x-5,6 Objectives is based on the formula relating the horizontal and vertical resolution (e.g. Kurinski 1997), the vertical resolution being determined by a 100 Hz sampling rate in the neutral atmosphere.

G40.x.x-9,10 Based on model parameters in the vertical coverage ranges.

G40.x.x-13,14,15 Threshold based on 1K accuracy obtainable with the GPS/MET experiment. Objectives based on preliminary simulations.

G40.x.x-17 Based on the horizontal cell size and the number of useful occultations (about 3200 per day) produced by 3 satellites.